Analysis and Design of Resonant Inductively Coupled Circuits: Application to Benefit Denial Solutions for the Retail Industry

by

Amaury Rony

B.S. Mechanical Engineering

Ecole des Ponts Paristech, 2011

Submitted to the Department of Mechanical Engineering
in partial fulfillment of the requirements for the degree of

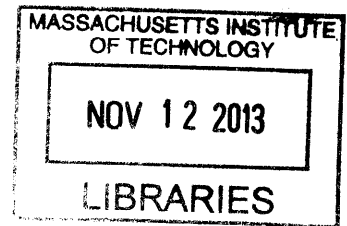MASTER OF ENGINEERING IN MANUFACTURING

AT THE

MASSACHUSETTS INSTITUTE OF TECHNOLOGY

September 2013

©2013 Amaury Rony. All rights reserved.

Signature of Author: . . . . . .

Amaury Rony

Department of Mechanical Engineering

August 15, 2013

Certified By: . . . .

Prof. David E. Hardt

Ralph E. and Eloise F. Cross Professor of Mechanical Engineering

Thesis Supervisor

Accepted By: . . . . . .

Chairman, Committee for Graduate Students

Department of Mechanical Engineering

This page is intentionally left blank

Analysis and Design of Resonant Inductively Coupled Circuits: Application to Benefit Denial Solutions for the Retail Industry

by

Amaury Rony

Submitted to the Department of Mechanical Engineering
in partial fulfillment of the requirements for the degree of
Master of Engineering in Manufacturing

Abstract

ProTeqt develops benefit denial solutions that are electromagnetically deactivated. A magnetic field from the deactivation tablet inductively heats an enabler that provides the proper force to disengage the locking mechanism. Its latest design was not functional at one inch above the deactivation tablet, because of significant efficiency losses in the electromagnetic energy transfer. This is problematic when the product's package is thick. In order to improve the maximal functional distance, an LC circuit is inserted inside the locking device. This thesis describes the optimization and integration of the circuit, used as a weakly coupled electromagnetic resonator in wireless energy transfer. The most efficient resonator design is proposed, under the inherent constraints of this application. It is then tested in real situation in order to evaluate the failure rate of the complete device. Some modifications of the enabler are proposed and discussed to maximize the reliability. Finally, a simulation is conducted to test the sensitivity of the results to the circuit manufacturing variability. Under several clearly stated assumptions, it appears that the manufacturing variability of the hand-made enabler is the most significant, although it does not threaten the reliability of the current locking mechanism.

Thesis Supervisor: David E. Hardt
Title: Professor of Mechanical Engineering

Acknowledgements

First of all, I want to thank my excellent teammates: Mitch Krogman and Tianyu Zhu. They brought great ideas all along the project and I heavily benefited from their different backgrounds to learn something new almost every day.

I am very grateful to Dan Bean, senior mechanical engineer at ProTeqt. During the entire project, he was extraordinary available and helpful. Despite the fast-pace at which every start-up runs, he always found time to respond to our numerous inquiries and provide us with valuable information.

Many thanks to Dr. David Hardt, my adviser. He was always there to answer our questions and question our certitudes. I really appreciated that he kept the door of his office open to help us overcome all the obstacles we faced.

I also give thanks to all the ProTeqt's staff and affiliates: John Berg and George Raniuk who proposed and launched this internship, John LaMalva who introduced us to ProTeqt's marketing, Dimitar Bentchev for his help over the lock mechanism and Stephen Kusy who always knew where the missing tool for each of our experiments was.

I thank Jenifer Craig for carefully following up the writing progress of this thesis. Thanks also to Jose Pacheco who managed the logistics of the MEngM internships (and fed us so often).

Last, but far from least, I express my huge gratitude to my parents and all the people who supported me during this year at MIT. I dedicate my thesis and all my work to them.

Table of Contents

List of Figures

9

List of Tables

Chapter 1

Introduction

1.1.   General Research Topic

The foundation of this thesis is centered on ProTeqt Technologies, a company dedicated to providing anti-theft devices (known as "benefit denial solutions") for the electronics retail industry. In particular, we are developing a technique that can be used to expand their product functionality, based upon a mechanical locking mechanism for a Micro USB hub. More explicitly, we are developing components and understanding parameters that will increase the distance from a disabling device their technology can be used by extending a magnetic field via resonant coupling.

1.2.   Need for Benefit Denial Solutions against Retail Theft

Global retail theft has increased dramatically in recent years, driven by the expansion of online marketplaces [1]. Large online market places such as EBay have given rise to organized retail theft. These online markets make buying and selling stolen items easier than ever. Despite huge investments from retailers and manufacturers (more than $28 billion in 2011 [2]), this plague has continued to grow steadily. The most common solution to prevent theft in retail stores is an electronic article surveillance (EAS) system that alerts the retailer if a product passes through the doors prior to purchase. EAS systems have the limitation that the retailer still has to respond to the alert and this response is often hesitant. In some cases, retailers explicitly tell their employees not to confront those suspected of theft. Increased shrinkage, coupled with non-effective EAS systems, has lead retailers to restrict consumer access for high-theft products (e.g. locking glass or back room cages). However, these actions are known to significantly decrease sales. Moreover, these solutions attempt to address theft only at the point of sale. They fail to address the largest component of shrinkage in the retail industry: organized theft throughout the supply chain (53% of theft in North America [2]).

As a result, retailers are looking for solutions that will provide more security than current theft prevention methods. They are interested in eliminating the motivation to steal: the resale or use of the product. ProTeqt Technologies has addressed this solution by developing a new type of mechanical lock system that temporarily disables the product, rendering it unusable until it is legally

purchased. At the point-of-sale, a deactivating tablet recognizes the product using a RFID tag embedded in the packaging. It then emits a certain electromagnetic signal, based on the product, that deactivates the mechanical lock. If the product is stolen, the lock cannot be removed without damaging the product. Furthermore, their solution can also be easily integrated with current EAS systems using existing RFID tag.

1.3.   Product Components and Performance

ProTeqt's system is comprised of three key elements: the deactivation tablet, cloud database, and mechanical lock. The research covered by this thesis focuses on two of the three elements: the deactivation tablet and the mechanical lock. However, to fully understand ProTeqt's technology and the sequence of events that takes place, we must briefly consider all three elements.

At the point of sale, the sales clerk first scans the product containing the ProTeqt's lock. The RFID is then recognized, allowing the system to look in the ProTeqt database for data corresponding to that particular product. If the product has not previously been unlocked, a certain frequency is taken from the cloud database that coincides with the product at hand. The clerk then positions the product in such a way that the lock is directly over the center of the tablet. With the product in position, the tablet creates a strong electromagnetic field at the appropriate frequency to deactivate the mechanical lock. The customer takes the product home, and uses his or her product as if the lock was never there. They are able to simply remove the lock and throw it away.

1.3.1. Deactivation Tablet

The deactivation tablet is a highly integrated computer system. The system uses RFID detection to recognize products, an Internet connection to access the cloud database, LED lights to guide the product to the center of the tablet, a function generator to produce certain frequencies, and finally a large coil to generate an electromagnetic field. The tablet must be small and unobtrusive, to provide easy integration at the point of sale.

ProTeqt has contracted the design and manufacturing of the deactivation tablet to MACK Technologies[1], whose expertise is in circuit board and complex system assembly. While we may not be designing, or analyzing the system for manufacturability, we need to understand the full

---

[1] www.macktech.com

functionality and design parameters of the deactivation tablet to further understand the effects it has on other components like the mechanical lock.

1.3.2. Mechanical Lock

The mechanical lock is a small device that is added to a consumer product in a manufacturing stage. The lock is designed to eliminate key features of a product. By encapsulating and interacting with the consumer product, both internally and externally, the device is completely protected from use if not legally purchased. Inside, the lock contains a mechanism that will disengage itself from the internal portion of the consumer product. When disengaged, a spring pops the lock off the product inside the packaging. This action is completed at the point of sale, when the lock receives the proper magnetic field. The deactivation mechanism is explained with more details in chapter 6.

The lock design is highly dependent on key product features that can be used to render the product unusable. At the time of this project, locks have been designed for two product lines: USB thumb drives and CD-type disks (See Figure 1). For the USB thumb drives, the lock is attached to the male plug. An improper attempt to remove the lock will permanently damage the plug, rendering the USB drive useless. For the disks, the lock secures the disk to its case. Here, improper removal will simply break the disk.

Figure 1: The thumb drive lock (Left) and the CD-disk lock (right). Locking mechanisms are signified by the pad-lock symbol.

1.3.3. Improving Product Performance

ProTeqt has complete control over their mechanical locking device and deactivation tablet, but they must be compatible with numerous types of locking methods (e.g. USB, disk, etc.) and packaging. In the case of the USB thumb drives and the disks, the packaging is very slim, allowing the lock to be close to the deactivation tablet. Once the magnetic field is created, the lock is easily deactivated. Because magnetic fields degrade at distance, products that are embedded in thicker packaging (Figure 2) have proven to be more difficult to unlock. ProTeqt has begun to investigate solutions that will provide deactivation of the mechanical locks at a distance of 1 inch from the tablet.

ProTeqt, having developed two unique applications for their technology (USB thumb drive, and CD-type disk), is ready to move forward in the development for a new Micro USB lock. This lock will perform similarly to the USB thumb drive lock, in that it will interface with the consumer product both internally and externally. The Micro USB hub uses a smaller profile than the standard USB hub, introducing some new design challenges. However, the Micro USB lock is used far more prevalently and with more expensive products than the standard USB. Moving forward, ProTeqt would like to achieve the functionality of the Micro USB lock at 1 inch above the tablet surface.
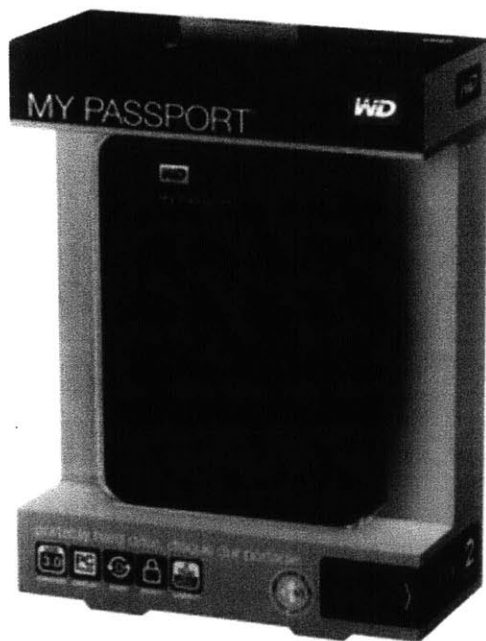
Figure 2: External hard drive with packaging requires a stronger field. This packaging, being targeted by ProTeqt, leaves the lock at 1 inch above the tablet.

1.4.　　Resonant Coupling

As stated above, the objective of ProTeqt is to achieve unlocking at one inch from the tablet. Among several potential solutions, ProTeqt chose to explore and implement the effects of resonant inductive coupling. Resonant inductive coupling is a means to transfer wireless energy through two coils that are tuned to resonate at the same frequency. We can effectively use resonant inductive coupling to extend the magnetic field created by the deactivation tablet. Moving the field closer to the mechanical lock will increase the effectiveness of the field at distance. Furthermore, this solution allows ProTeqt to postpone a redesign of the deactivation tablet. Instead, a simple component can be designed that will allow the wireless transfer of energy: an LC circuit.

1.5.　　Design and Production of LC Circuits

To extend the field, we need to develop an LC circuit. An LC circuit is a circuit comprised of an inductor and a capacitor. This circuit is typically drawn as shown in the figure below (**Error! Reference source not found.**). By placing the small circuit inside the mechanical lock, we can extend the magnetic field so that it is actually formed inside the lock. Although an LC circuit is simple (an inductor coil connected to a capacitor), it must be designed to work at maximum efficiency. The circuit can be tuned to operate most efficiently at a certain frequency. However, because the LC circuit will be operating inside the mechanical lock, we must consider the interaction and effects of the existing components of the lock.
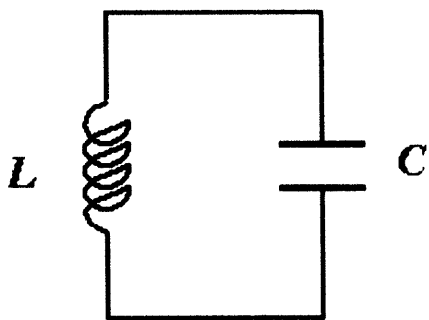
Figure 3: Typical diagram for an LC circuit where L is the inductor and C is the capacitor

Moreover, the performance of the circuit is dependent on the quality of manufacturing. Thus, the effects of manufacturing variability must be understood, controlled, and minimized.

Finally, as the circuit is inside the lock, it is disposable and must be manufactured at low cost, and on the order of millions of units per year. The production rate and cost are two important parameters that must be considered and optimized from the very beginning of the design.

1.6.   Problem Statement

The goal of this project is to develop the initial idea of a field repeater using resonant inductive coupling. There were multiple challenges, from theoretical physics to manufacturing issues. This thesis only considers those we faced while working at ProTeqt. It must be noted that some tasks were distributed among ProTeqt's partners and are out of the scope of this thesis.

This project was conducted through three phases. First it was necessary to understand the principle of radio frequency heating, physical mechanisms of a field repeater, and optimizing the design of an LC circuit. We focused especially on the coil and LC circuit. For purposes of testing, it was easier and more flexible to design for a wire coil. Preliminary experiments were conducted to characterize the circuit: (1) the geometry and the shape of the coil, (2) the design parameters (number of turns, wire gage and number of layers), (2) the capacitance, and (3) the resonant coupling efficiency. From this study, a second design was proposed for the manufacturing processes that can only achieve thin conductive lines (i.e. high resistance).

In the second phase, the unlocking mechanism is analyzed to understand the interaction between the mechanical parts and the electronic circuit. The purpose of this stage is to guarantee the reliability of the product after inserting the LC circuit.

Finally, in the last phase of the project, different manufacturing methods were investigated: winding, etching, screen printing and inkjet printing. They were analyzed according to three criteria: (1) feasibility of the design, (2) production rate capability, and (3) production cost. Following this analysis we need to define and understand the manufacturing processes and techniques that would be appropriate to produce the circuit, given our constraints. For each of these steps, we highlight the key decision factors and provide recommendations.

1.7.   Task Division

Based upon the three phases of the approach, tasks were divided among the three group members: Mitchell Krogman, Amaury Rony, and Tianyu Zhu. Even though the thesis project at hand has been completed by the collective group, each team member took the lead on one of the three phases, and

delegating responsibility for tasks essential to completion as needed. Theoretical physics and coil design was under the responsibility of Amaury Rony. Mitchell Krogman led the work on the unlocking mechanism and its interaction with the LC circuit. Finally, Tianyu Zhu took responsibility of the manufacturing process analysis and selection.

Chapter 2

Electromagnetism and Inductive Coupling

2.1.   Magnetic Field Due to Current

This section intends to give the minimal background about Electromagnetic theory that is necessary to understand inductive coupling. For more extensive information, the reader is invited to refer to a detailed handbook like [3]. To illustrate the principles of induction, we first present the principles of induction heating. Even though the project covered by this thesis does not focus on this heating method, this is the fundamental principle for every lock at ProTeqt.

Induction heating is a method to heat an electrically conducting object using electromagnetic induction. An inductive heater consists of an inductor excited with an alternating current. According to Faraday's Law, such changing current creates a changing electromagnetic field around the inductor. When the electrically conducting object is placed inside this field, eddy currents are generated within the conductor. This phenomenon causes Joule heating, owing to losses in the conductor. Compared to traditional heating method, induction heating does not require direct physical contact as the energy is transferred through electromagnetic waves.

2.1.1. Eddy Currents

French scientist François Arago first discovered eddy currents in 1824 [4]. When a conductor is placed in a changing magnetic field, circulating eddies of current are created inside the conductor. The name eddy current comes from the analogy of circulating water in fluid dynamics. In a non-zero resistivity conductor, the eddy current induced will generate Joule heating and electromagnetic forces. The current will become greater with either a stronger magnetic field or a higher frequency magnetic field. According Lenz's law, the eddy current will flow in a direction such that the magnetic field created by the current will oppose the magnetic field that induces the current. In another word, the eddy current will create a magnetic field to cancel part of the external field.

2.1.2. Skin Effect

With direct current, current density is uniform through the entire cross section of the conductor. When the current becomes alternating, the magnetic field at the center of the conductor increases as the frequency increases, due to the combined effect of conductivity and permeability. The magnetic field creates a current in the opposite direction of the current flowing through, making it more difficult for the current to flow in the center. This is called reactance. Because of the reactance at the center, the current density is the lowest there and the largest near the surface of the conductor, where the reactance goes to zero. This concentration of current at the surface is named the "Skin Effect".
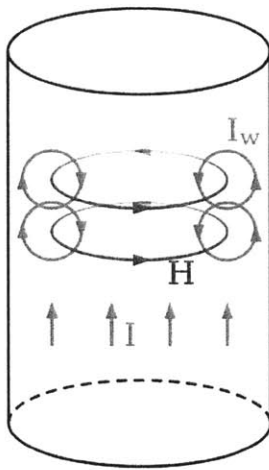
Figure 4: Schematics drawing of current and magnetic field in a conductor with alternating current. I (red arrows) is the current passing thought the conductor. It induces the magnetic field H (blue loops), which itself creates the loops of current I_w

In order to acknowledge the skin effect on the resistance of the conductor, the skin depth needs to be estimated [5]. The AC current density decreases exponentially with the depth from the surface. The skin depth is defined as the distance into a conductor at which is current density falls to $\frac{1}{e} \cong 37\%$ of its value along the surface. The skin depth can be expressed as:

$$\delta = \frac{1}{\sqrt{\pi f \mu \sigma}}$$

(2.1)

where f is the frequency of the current, $\mu = \mu_r \mu_0$ is the absolute permeability of the medium[2] and σ is the conductivity of the material.

---

[2] $\mu_0 = 4\pi \times 10^{-7} H/m$. μ_r is the relative permeability of the medium.

For example, for a copper wire carrying an AC current of 220 kHz, the skin depth is 0.141mm. It means that 63% of the current flowing in a copper wire will flow within a distance of 0.141mm to the surface. The effective resistance can be calculated as current flowing uniformly through a layer of thickness δ with the DC resistivity of that material. The effective cross-sectional area can be approximately represented by:

$$A_{eff} = 2\pi r \cdot \delta \tag{2.2}$$

where r is the radius of the wire.

Then, the AC resistance is:

$$R_{AC} \approx R_{DC} \frac{r}{2\delta} \tag{2.3}$$

All the equations shown above are based on the assumption that the skin depth is significantly smaller than the radius. If the skin depth has the same order of magnitude as the wire radius, the AC resistance at low frequency (below 1 MHz) can be calculated using the following equation:

$$R_{low\,freq} \approx R_{dc} + \frac{l}{48\sigma\pi\delta^2} \tag{2.4}$$

where l is the total length of the wire.

The first consequence of the skin effect is the increase of resistance, as the skin depth decreases. The value of skin depth is inversely proportional to the square root of the current frequency and the material permeability (see eq. 2.1). Depending on the application, a small skin depth may be an advantage or disadvantage. For instance, if the skin depth is small there will be a large effective resistance. If the goal is maximizing current flow this is a disadvantage, but if the goal is Joule heating (as is the case here) a small skin depth is an advantage. To maximize Joule heating two design strategies can be considered: the selection of materials and thickness.

2.1.3. Selection of Materials and Thickness

The selection of material is critical for the effectiveness of heating. Only conductive materials can be used for induction heating because eddy current needs to flow in the object to generate heat. Even though eddy currents can occur in any conductor, iron and its alloys respond better than aluminum and copper to induction heating owing to their ferromagnetic nature. With same alternating current,

ferromagnetic materials have significantly smaller skin depth, resulting greater resistance. Therefore, more Joule heat is created.

For materials that are thinner than their skin depth at the desired frequency, the skin effect is no longer important. The resistance of the material is only determined by the thickness and the material resistivity. In this case, aluminum and copper can perform just as well as iron.

2.2.   Magnetic Field in a Coil

2.2.1. Magnetic Field Strength at a Coil Axis

Every current, i.e. a flow of moving charges, is associated with a magnetic field. This magnetic field magnitude is represented by the magnetic field strength $\vec{B}$ (in Teslas). The magnetic field generated by a line current within a wire is derived from Biot-Savart law [3]. That is

$$\overrightarrow{B_Q} = \frac{\mu}{4\pi} \int_L \frac{\vec{I}dl \times \overrightarrow{\iota_{QP}}}{QP^2} \tag{2.5}$$

Q is the point of observation.

P is the center of the elementary element dl.

$\vec{I}$ indicated the intensity and the direction of the current at P.

$\overrightarrow{\iota_{QP}}$ is an elementary vector from Q to P.

μ is the absolute permeability of the medium

From this equation, it is possible to find the magnetic field along a single circular loop of radius a and that carries a current I. We are especially interested in the magnetic field $\overrightarrow{B_z}$ along the axis of the loop. It is oriented in the axis direction, as shown on Figure 5:
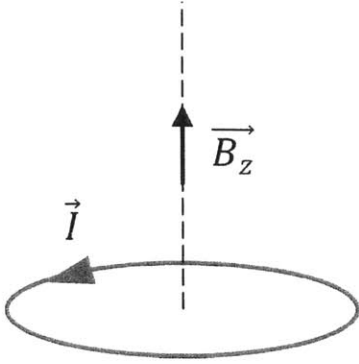
Figure 5: Current-carrying Loop and associated magnetic field along the central axis

The magnitude of the field is

$$B_z = |\overrightarrow{B_z}| = \frac{\mu I a^2}{2(z^2 + a^2)^{\frac{3}{2}}}$$ (2.6)

To understand the effect of distance, the magnetic density from eq. (2.6) is plotted as a function of the distance from the loop, with a = 1mm and I = 1A (see Figure 6).
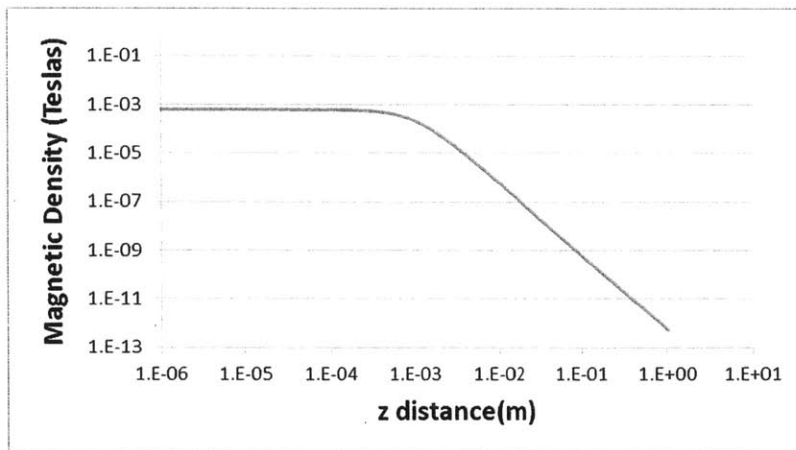
Figure 6: Magnetic Field along the loop axis, versus the loop radius (log-log scale). Loop radius is 1 mm and current is 1 A in eq. (2.6).

As long as the distance from the conductor is smaller than the radius, the magnetic field remains approximately constant. However the magnetic density decreases rapidly as the measuring point is

moved further away from the center of the loop. In free space, the decay is 60 dB per decade. It has been shown experimentally that the slope flattens out to 20 dB per decade in the far field [6].

As will be discussed below, a flat spiral coil can be used to increase the magnetic field by increasing the number of loops. A spiral coil can be seen as a certain number of concentric loops with different radii $(a_1, a_2, a_3...)$, and potentially with N layers. In this case, the total intensity of the magnetic field along the axis of the coil is the superposition of the magnetic field intensities generated by each single loop [6].

$$B_z = \sum_N \sum_i \frac{\mu I a_i^2}{2(z^2 + a_i^2)^{\frac{3}{2}}}$$ (2.7)

The magnetic field is often associated with another field, closely related to $\vec{B}$: the *magnetic strength* $\vec{H}$ (in Ampere per meter). For the purpose of this thesis, we do not consider the magnetization of the material. In this case, both fields are proportional:

$$\vec{B} = \mu_r \mu_0 \vec{H}$$ (2.8)

For air, $\mu_r \cong 1.$ [3]

2.2.2. Magnetic Flux and Inductance

The line along which the magnetic strength is constant is called *line of magnetic flux*. We are interested in the *magnetic flux*, i.e. the total number of flux lines passing through a given surface. The magnetic flux Φ is proportional to the field density B and the area:

$$\Phi = B.A$$ (2.9)

Going back to the current-carrying loop, it is now possible to define and calculate its inductance L.

$$L = \frac{\Phi}{I}$$ (2.10)

where Φ is the magnetic flux through the inside surface of the loop.

According to eq. (2.6) and (2.9), the magnetic flux is

---

[3] $\mu_r = 1.000\ 000\ 37$

$$\Phi = \frac{\mu I a^2}{2a^3} \times \pi a^2 \qquad (2.11)$$

Thus, the inductance of the loop is

$$L = \frac{\mu \pi a}{2} \qquad (2.12)$$

It is noticed that inductance does not depend on the current. It only depends on the material properties and the geometry layout. This remains true for more complicated inductors. According to eq. (2.7) and (2.9), the inductance of a spiral coil is the sum of the inductances of each single loop.

2.3.   Inductive Coupling

If a second conductor loop is located close to the first one, a portion of the magnetic flux Φ_{21} from the first loop is passing through the second one. The two conductors are now coupled. As for inductance (also known as self-inductance), we define the mutual inductance M_{21} of conductor loop 2 in relation with conductor loop 1 as:

$$M_{21} = \frac{\Phi_{21}}{I_1} \qquad (2.13)$$

In a similar way the mutual inductance of conductor loop 1 in relation with conductor loop 2 is

$$M_{12} = \frac{\Phi_{12}}{I_2} \qquad (2.14)$$

It has been shown that both mutual inductances are equal [6] i.e.

$$M_{12} = M_{21} = M \qquad (2.15)$$

The mutual inductance gives a sense of the quality of coupling between the two inductors. In order to make it independent of their geometric characteristics, the *coupling coefficient k* is introduced:

$$k = \frac{M}{\sqrt{L_1 L_2}} \qquad (2.16)$$

where L_1 and L_2 are respectively the self-inductance of the primary and the secondary inductors.

Continuing with these two coils, we consider the case where the first one carries a high frequency current, producing varying magnetic field at the same frequency. The other coil (*secondary coil*) is located in the surrounding area so that they are coupled. Faraday's law states that any change to the magnetic flux generates an electric field. This electric field induces a voltage in the secondary coil.

In order to formalize this result, it is assumed that each coil consists of one loop for radius a_1 and a_2 respectively. The primary coil carries an AC current i_1, generated by an ideal voltage source E. The secondary coil is connected to a load R_L. The resistance of the secondary coil is R_2. Let be u_2 the voltage across the load of the secondary circuit. The schematic circuit is given on Figure 7.
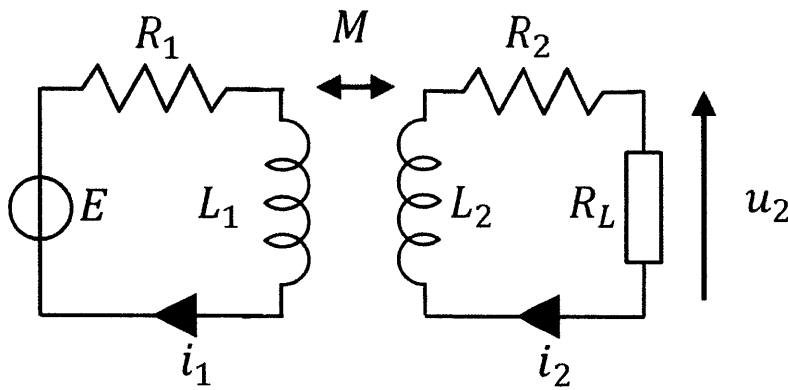
Figure 7: Electric circuit of the coupling

Faraday's law integral form is

$$\oint_L \vec{E}.\overrightarrow{dl} = -\frac{d\Phi}{dt}$$

Thus,

$$u_2 = L_2 \frac{di_2}{dt} + R_2 i_2 - M \frac{di_1}{dt} \qquad (2.17)$$

$L_2 \frac{di_2}{dt}$ is induced by the magnetic flux from the secondary coil itself, whereas $M \frac{di_1}{dt}$ is induced by the magnetic flux from the primary coil. These two voltages are of opposite signs. Indeed, Lenz's law states that the direction of induced current is always such as to oppose any change in the magnetic flux already present. Thus both fluxes are in opposite direction.

Finally, we assume sinusoidal alternating current and continue calculation with complex notation.

$$u_2 = j\omega L_2 i_2 + R_2 i_2 - j\omega M i_1 \qquad (2.18)$$

Replacing i_2 by u_2/R_L,

$$u_2 = -\frac{j\omega M i_1}{1 + \dfrac{j\omega L_2 + R_2}{R_L}} \qquad (2.19)$$

This induced voltage can be used to supply power to another application (RFID chip, transformer ...).

2.4.   Resonant Coupling

Experience and analysis [7] show that coupling decreases very quickly when distance between coils increases. That is why transformer coils are installed as close as possible.

In the apparatus described above, the resistive load is replaced by a capacitance C_2. This new coupling exhibits a resonance phenomenon at a certain frequency. This is visible by plotting induced voltage versus frequency of the current source, all other parameters remaining fixed (Figure 8).
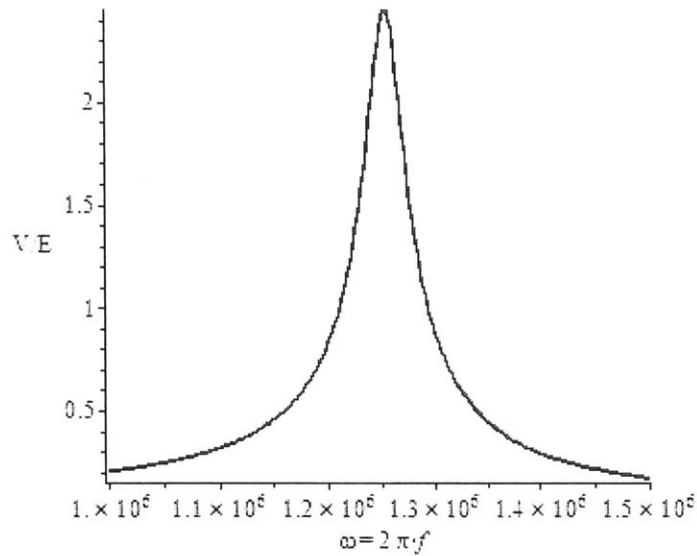
Figure 8: Voltage gain versus frequency, for a coupling coefficient k = 0.1. This figure was plotted from equations derived in section 4.1, where $u_2 = V$.

At this frequency, called *resonant* or *natural frequency*, the power transmission is much more efficient. Thus, the distance between the coils can be substantially increased.

2.5. Applications

This physical phenomenon can be advantageously used for contactless applications. We present two of the most important: RFID tags and wireless power. Both applications are used by ProTeqt. Before the deactivation of the lock, the product is recognized by its RFID tag, inside the package. Then, the principles of wireless power transmission will be used in order to increase the maximum distance of deactivation.

2.5.1. RFID

Nowadays lots of company make a massive use of automatic identification systems, or Auto-ID, for a large range of applications: inventory management, sales and purchase, payment, safety controls, communication ... The most widely used are the barcode and the smartcard. Among all the available solutions, RFID systems (for Radio Frequency Identification) have three major advantages: identification is passive, contactless and reconfigurable. Like smart cards, data is stored on an electronic data-carrying device, called the *chip*. However, RFID devices do not require physical contact between the chip and the *reader*. Instead, data exchange is achieved using electromagnetic field. The electromagnetic waves are

29

emitted and received through two coils (or *antennas*), one is connected to the chip and the other one is in the reader. The device made by the antenna and the chip is called *transponder*.

To maximize the power transmission and thus the working distance between the transponder and the reader, the resonant frequency of the system is used to convey information. Two kinds of systems can be distinguished: passive and active transponders. A passive transponder does not provide any energy and only receives it from the reader's magnetic field. This energy results in a change in the impedance of the transponder. This shifts the initial natural frequency of the system, which is detected by the reader. On the opposite, active transponders carry a battery. They can transmit their ID signal using their own energy source. The signal is sent either periodically or in the presence of an RFID reader. Passive transponders are more widely used, mainly because they are less expensive. The advantage of active transponders is that they work at higher distance [6].

2.5.2. Wireless Power

Wireless energy transfer is as old as alternating current [8]. The transformers are ubiquitous in most electronic devices and indeed in all electricity distribution network transfer energy by using mutual inductance. In recent years, wireless energy transfer for an array of applications has become an increasingly investigated use of resonant inductive coupling. A team of physicists at MIT has worked on this subject since 2005 [9,10]. They realized that resonant objects tend to couple, whereas off-resonant interaction remains extremely weak. Thus, energy transfer efficiency between two resonators increases with the coupling level between them. It is called non-radiative wireless energy transfer. In terms of energy transfer, non-radiative transfer is much more interesting than other solutions, such as radiative transfer (huge loss) or directed radiation modes (that requires uninterruptible line-of-sight). Some foreseen applications are:

- Charging portable electronic devices by placing it within the source field
- Supplying power to mobile robots and machines in a factory
- Supplying power to internal medical device (pacemaker, medicine delivering devices ...)

Over the years, several designs have been tested and refined. For now, the highest efficiency has been achieved with a four-coil apparatus: the power supply with an inductor, first resonator, second resonator, and the receiver with the device to power (e.g. a light bulb). A schematic of the system is given in Figure 9.
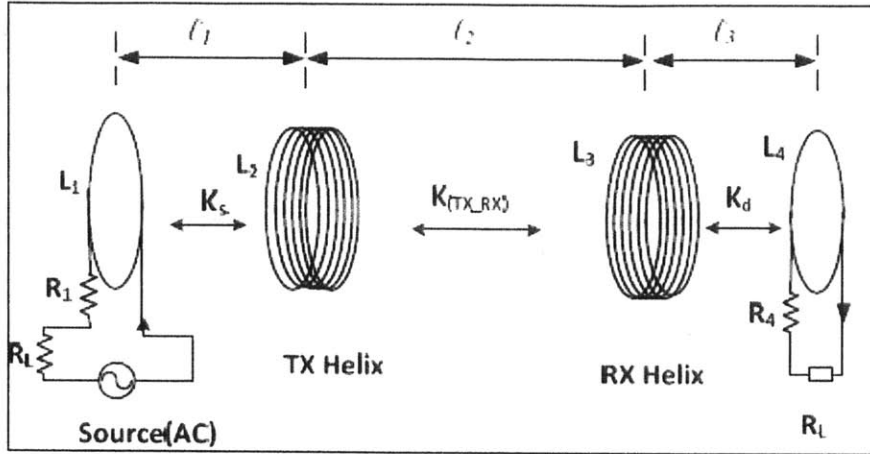
Figure 9: Typical Strongly Coupled Magnetic Resonance (SCMR) System. TX is the transmitting helix. RX is the receiving helix.
[11]

Resonant inductive coupling only happens between the two resonators. The transmitting helix is inductively coupled with the source loop. Similarly, the receiving helix is inductively coupled with the load loop. With this system, several promising achievements have been reached. It is able to provide more than 90% efficiency at 15 cm distance. At a distance of 2 m, it can achieve an efficiency of 40% for single receiver and up to 60% for multiple receivers. Recently, the research team, now a company called *Witricity*, introduced a repeater to extend the magnetic field further, and thus reach higher transfer distance. This repeater inserts another resonators in between the two previous ones (transmitting and receiving helixes) [10–12].

Chapter 3

LC Circuit Manufacturing

Proteqt had previously determined that an LC circuit with a resonant frequency in the range of xxxx would be necessary for distance activation. This circuit would be part of each device , and therefore must be compact enough to fit in the locking device and inexpensive enough to keep the device cost low. These requirements make the design and manufacture of this circuit critical to the success of this product. In this chapter we examine a variety of methods for making such a device.

3.1.   Inductor Manufacturing

An inductor, in its simplest form is a coil of wire used to resist a non-constant current flow [13]. It stores energy in a magnetic field created by current flowing through a coil. Inductors can come in many shapes and sizes. These parameters often affect inductor performance [14]. The magnetic field created by inductor is very dependent on inductor shape, whereas the intensity of the field is determined by the number of turns within the coil. For our application we are interested in designs that will permit an electromagnetic field extension through resonant coupling. Materials are especially important in inductors. The time required to establish a magnetic field is proportional to the coil resistance [13]. High current is desirable to quickly set up a magnetic field. Changing the linear length of the coil, or the coil's material properties can alter resistance, and therefore the field [14]. High coil resistance will also result in heating, and therefore promotes energy loss.

For this project, three inductor-manufacturing methods were analyzed: chemical etching, coil winding and screen printing. After consulting ProTeqt's manufacturing partner, MeadWestVaco, winding was deemed the least expensive method to make coils quickly and repeatably. However, other methods may be considered for two reasons:

- If they can achieve better energy transmission between the primary and secondary coils, or
- If they become more competitive in the near future.

3.1.1. Chemical Etching

Chemical etching is a controlled material removal process that uses a resist to prevent portions of a material from being removed by a chemical etchant. Once the resist is removed, a desired pattern remains. The process at hand uses copper and a resist to etch a copper pattern.

Before Etch

Resist

Copper

Laminate

After Etch

Resist

Copper   Copper

Laminate
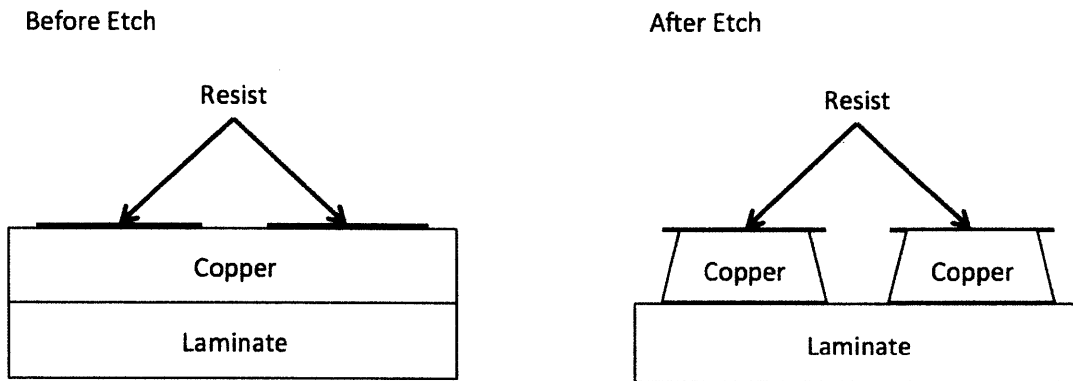
Figure 10: Schematic of a typical etching process.

Figure 10 explains how chemical etching works [15]. You will notice that the etchant removes material in two directions, not just vertically. That is, a slight angle is apparent in the final product because the etchant is in contact with that portion of the material after it passes beyond the resist. Finally, it's important to not that this is a chemical material removal process. Meaning the copper that is removed cannot be easily recycled, making the process as a whole, inefficient.

Etching allows for batch processing of inductors however, restricts coil designs to single layer, flat spiral coils. Economical etching is usually done in large batches of very thin materials. These materials are often on the order of 0.03mm thick [15]. As material thickness increases, time to etch increases. This property is inefficient in terms of processing energy. This directly impacts the production cost.

As material thickness decreases, resistance increases. This resistance restricts current flow through the material, and therefore increases the amount of voltage needed to create an electromagnetic field. The time requirement to etch thick pieces of copper (0.5mm) is about 5 minutes [16]. This however is not what limits the chemical etching process in terms of this application. The limiting factor is in the material costs. Copper is very expensive, and is only one of the materials used in the

process. Resist and the chemical etchant also need to be purchased, along with the many cleaning solutions used to remove the etchant.

3.1.2. Coil Winding

Coil winding is a process that bends a wire (usually radially) into a desired shape. This can be done manually or automatically, and many different winding patterns can be achieved. This process bodes well for inductor manufacturing because an inductor, in its most basic form, is a wound coil. Size and shape of the coil, and wire used to create the coil can impact the inductor performance. Wound coils can be formed into almost any desired shape including flat spiral, cylindrical, rectangular, etc. Wire geometry is often limited by market availability. Rectangular and circular cross sectional wire are most common. Wires are found most commonly in certain AWG gage sizes, which have a circular cross section. Diameters are fully customizable depending on the type of winding machine. Usually machines can operate using a range of wires. Automatic machines often integrate several functions including dispensing, winding, and cutting the wire. Machines can accommodate simultaneous coil winding, providing a batch process. Batch processing allows the machines to produce coils at a high rate.

The cost of wire is very low compared to copper foils (used in etching). Wire is packaged as a large spool that is fed into the coil winding machine. Because the wire is continuous, there is almost no waste and the two ends of each coil are left exposed, ready to be soldered to the remaining capacitor.

3.1.3. Screen Printing

Screen printing is a highly integrated manufacturing process that can provide an entire LC circuit in one process. The process uses a mask that contains the circuit pattern. Conductive ink is then deposited on the mask, and the circuit is printed on the areas not protected. Silver and Aluminum are the most popular conductive inks used in this process. Dielectric materials can also be used to print capacitors. This is done in layers. First a conductive layer is deposited, followed by a dielectric, and finally another conductive layer. [17]

The flexibility of screen printing is similar to that of chemical etching. It is commonly used for making flat, flexible circuits. The deposited layers are very thin (40 micron), but can be built up in layers. Building layers requires more processing time, and is therefore less economical. The thin nature of screen printing causes inherently high resistance values. Capacitors are printed as large flat surfaces,

requiring a large amount of surface area. Spacing is also critical in screen printing. The silver ink does not have an insulating coating, so line spacing also requires more space. Like chemical etching, large batches can be printed at once. However, screen printing requires no post processing because the capacitor can be printed as part of the circuit. [17]

The screen printing process is new relative to processes like etching or winding. While the added flexibility and integrated components are great for circuit board design and manufacture, it is still a new processes, and therefore costly. Future developments are expected to lead to significant cost reduction, leaving it as a potential process for future manufacturing. [17]

3.2.   Capacitors

Capacitors are common electrical components used in many types of circuits. They consist of two conductive plates that are separated by a dielectric layer. This configuration allows capacitors to hold a charge. Capacitors come in many shapes and sizes due to their simple design (see Figure 11). Capacitors are made in extremely high volumes by expert manufactures. With their cost at $0.0074 per capacitor[4], ProTeqt will be purchasing capacitors to use within their circuit.
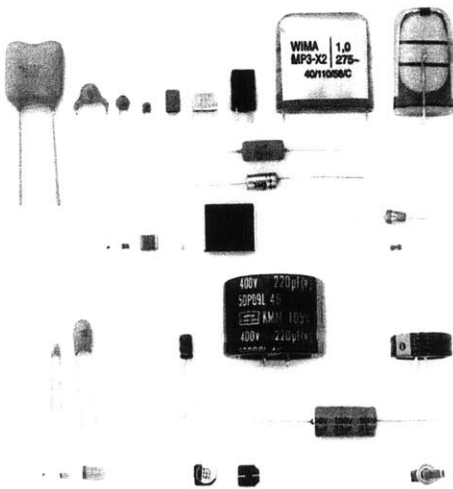
Figure 11: Typical shapes and sizes of capacitors.

Capacitor specifications usually include three key pieces of information: nominal capacitance and rated voltage. A capacitor will likely have these values printed on its side. A capacitor reading 1 μf

---

[4] Fenghua part number 0805CG9R0C500NT, quantity 10,000

20% at 100V, for example, will have a nominal capacitance of 1 microfarad with a tolerance of ± 20% (0.8µf – 1.2µf). Throughout the life of the capacitor, it should not handle more than 100 volts, as that is the rated voltage.

3.3. Soldering Techniques

Soldering is a method of joining two thin metals using a filler material. This filler material has a lower melting temperature than the two thin metal pieces, allowing the filler material to flow between, and bond to each of the thin metal pieces. The filler material is often made of tin and lead. Conductive properties allow soldering techniques to be prevalent in the electronics manufacturing industry, and especially circuit board manufacturing. Two common soldering methods are used in manufacturing today: robotic soldering and dip soldering.

Robotic soldering often uses a robot or other automation to control temperature and the feed rate of the filler material. Sophisticated control systems are used to gain a high level of precision over soldering processes. Robotic soldering often requires auxiliary tooling or methods of positioning and orienting components before they can be soldered.

Dip soldering is used more extensively for circuit board manufacturing. This process is used to solder several components simultaneously. Leads from electrical components protrude through the bottom of the printed circuit board. These are dipped into a lead-tin bath, where the solder then solidifies upon removal. [18]

Chapter 4

Physics of the Problem and Theoretical Analysis

This short chapter introduces some theoretical analysis of the resonant inductive coupling. In section 4.1, a formula is derived to find the secondary current with respects to the characteristics of the two circuits and the coupling coefficient. Then, in section 4.2, a theoretical optimal coil is proposed in order to limit the range of the experimental field.

4.1.   Analysis of the Coupling

In order to provide a better understanding of the problem, a theoretical analysis is proposed. The following calculations are directly adapted from [7]. First of all, we consider two spiral coils that are inductively coupled. The inductances of these coils are respectively L_1 and L_2. The primary coil is connected to a source of voltage $\underline{E}$ that generates a current $\underline{i_1}$:

$$\underline{E} = E e^{j2\pi f_0 t} \tag{4.1}$$

$$\underline{i_1} = I_1 e^{j2\pi f_0 t} \tag{4.2}$$

where f_0 is set to $220\ kHz$, the working frequency of the tablet

The secondary coil is connected to a capacitance C_2. Furthermore, the two coils are considered as a perfect inductance (resp. L_1 and L_2) in series with a resistance (resp. R_1 and R_2). This resistance is the resistance of the coil's copper wire. It is assumed that the total resistance of each circuit only consists of the coil's resistance. Figure 12 shows the diagram of the apparatus.
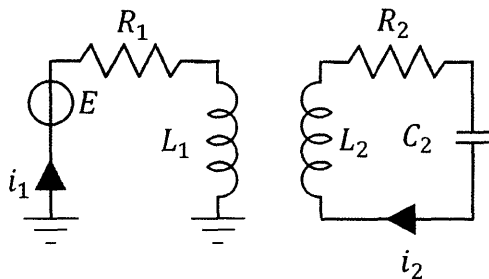
Figure 12: Diagram of the two coupled circuits. Primary circuit (left) and secondary circuit (right).

As explained in section 2, the current passing through the primary coil creates a magnetic field, which induces a voltage V_2 in the secondary circuit. This voltage depends on the mutual inductance (M) that represents the quality of the coupling.

$$V_2 = M \frac{di_1}{dt} \qquad (4.3)$$

Reciprocally, the secondary circuit then induces a voltage V_1 in the primary circuit:

$$V_1 = M \frac{di_2}{dt} \qquad (4.4)$$

where i_2 is the current passing through the secondary circuit.

As a result, the system is entirely defined by the two following relationships (given in complex notation):

$$(R_1 + j2\pi f_0 L_1)i_1 + j2\pi f_0 M i_2 = E \qquad (4.5)$$

and

$$\left(R_2 + j\left(2\pi f_0 L_2 - \frac{1}{2\pi f_0 C_2}\right)\right)i_2 + j2\pi f_0 M i_1 = 0 \qquad (4.6)$$

In order to simplify the equations, we introduce the impedance of each circuit:

$$Z_1 = R_1 + j2\pi f_0 L_1 \qquad (4.7)$$

$$Z_2 = R_2 + j\left(2\pi f_0 L_2 - \frac{1}{2\pi f_0 C_2}\right) \qquad (4.8)$$

Finally, combining equations (4.5) and (4.6),

$$i_2 = \frac{j2\pi f_0 M E}{Z_1 \cdot Z_2 + (2\pi f_0)^2 M^2} \qquad (4.9)$$

In order to achieve a resonant state between the two circuits, the secondary circuit is tuned so that

$$2\pi f_0 = \frac{1}{\sqrt{L_2 C_2}} \tag{4.10}$$

Moreover, the mutual inductance verifies $M = k\sqrt{L_1 L_2}$, with $0 \le k \le 1$ [6].

So, equation (4.9) becomes

$$\underline{i_2} = \frac{j\underline{E} \cdot k\sqrt{\frac{L_1}{C_2}}}{R_2\left(R_1 + jL_1/\sqrt{L_2 C_2}\right) + k^2 L_1/C_2} \tag{4.11}$$

Equation (4.11) gives an accurate idea of the physics of the problem. However, the coupling coefficient k is particularly difficult to evaluate. Some experimental methods have been developed to do so. The reader can refer to [7]. For the purpose of this thesis, the knowledge of k did not appear to be relevant. However, these equations give the general shape of the induced current versus the magnetic field frequency. Thus, they can be fitted to experimental data.

4.2.   Theoretical Optimization of the Coil

We can define coil efficiency as the amplitude of the magnetic field it can generate to heat up the enabler. The magnetic field is proportional to the current across the coil. Thus, we want to optimize the geometric characteristics of the coil, especially gage size and number of turns, in order to maximize induced current. In equation (4.11), the secondary current is a function of parameters that depend either on primary or secondary coil, or even on both, such as the coupling coefficient k. To simplify the expression of i_2, it is assumed that the primary coil generates a constant magnetic field, whatever the characteristics of the secondary coil. This magnetic field is vertical along the axis of the primary coil. At 1 inch above the center of the coil, its magnitude is $\underline{B}$. The induced voltage in the secondary circuit is now

$$\underline{V_2} = \sum_{i=1}^{N} a_i \frac{d\underline{B}}{dt} \tag{4.12}$$

where a_i is the area enclosed in the ith loop of the coil and N is the number of turns of the coil.

For ease of notation, we introduce the *geometric factor* $A = \sum_{i=1}^{N} a_i$. The defining relationship of the secondary circuit is now

39

$$Z_2 \cdot i_2 + A\frac{dB}{dt} = 0 \tag{4.13}$$

with Z_2 the impedance of the secondary circuit (see eq. 4.8) and i_2 the current passing through it.

Assuming $\underline{B} = Be^{j2\pi f_0 t}$, equation (4.13) becomes

$$Z_2 \cdot i_2 + j2\pi f_0 A\underline{B} = 0$$

$$i_2 = \frac{2\pi f_0 A\underline{B}}{Z_2} \tag{4.14}$$

If the secondary circuit is tuned to resonate at f_0, then $\underline{Z_2} = R_2$, so

$$i_2 = \frac{j2\pi f_0 A\underline{B}}{R_2} \tag{4.15}$$

And the modulus of i_2 is

$$I_2 = \frac{2\pi f_0 AB}{R_2} \tag{4.16}$$

Only A and R_2 depend on the secondary coil geometry. They can be determined from two characteristics of the coil: the wire gage and the number of turns. A spreadsheet has been written to evaluate the geometric factor and the resistance of the secondary coil, from the wire gage and the number of turns. The detail of this spreadsheet is given in appendix A.

Finally, the amplitude of the current in the secondary circuit is plotted with respects of the gage size and number of turns of the coil. As the value of the magnetic field amplitude was not known, the plot actually represents $I_2/|\underline{B}|$.
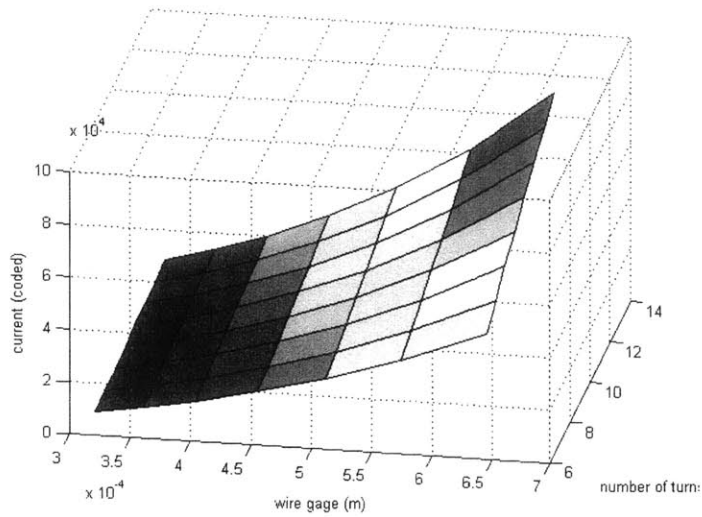
Figure 13: Current in the secondary circuit (coded unit) versus the number of turns and the gage size

Figure 13 shows that the most efficient coil has high number of turns and large wire gage. This conclusion has several limitations and must not be generalized outside the boundaries of the actual problem:

- The secondary coil must be significantly smaller than the primary one in order to assume that the coupling does not affect the primary magnetic field and that the magnetic field is constant through the secondary coil.
- There is no evidence that this conclusion would remain true at higher frequency than 500 kHz – 1 MHz

Before considering the geometric constraints inside the lock, this theoretical result is compared to a set of experiments conducted on different coils.

Chapter 5

Coil and Circuit Design

5.1.   Objective

The objective of this section is to provide design recommendation for the resonator inside the lock (LC circuit), in order to maximize the energy transfer from the tablet. First, some preliminary experiments were conducted to identify the significance of the parameters of the system, especially characteristics of the secondary coil (distance, number of turns, wire gage ...). Then a series of experiments were done at ProTeqt. The first step is to compare experimental results to the theoretical optimization conducted in section 4.2. The second one is to identify the various factors that modify the quality of the coupling between the two coils. This section always assumed a wound coil made of copper wire. This kind of coil is indeed much more flexible for experimental purposes. In order to extend this work to other manufacturing processes, this chapter also proposes an alternative design in the case of thin wires (when cross section area is below typical copper wires').

5.2.   Design Constraints

Before any other consideration, the final design must respect some geometric constraints. When we started this project, the design of the micro-USB lock housing had already been done. Only slight changes occurred for manufacturability reasons. Thus, the size of the coil should not exceed certain dimensions, in order to fit inside the lock. A specific location is made for the LC circuit. This space consists of two empty parallelepipeds, which are connected: one for the coil and one for the capacitor (see Appendix B). To fit this design, the diameter of the coil must be lower than or equal to 12.74 mm. As the available height is 1.143 mm, the wire diameter for a single layer coil must be lower than or equal to 0.551 mm. Indeed, the central end of the coil must pass above the rest of the coil to be connected to the capacitor.

5.3.   Experimental Apparatus

During the process of testing, the deactivator was still under development, and could not provide a controllable electromagnetic output. Inside the deactivator, there are an RFID reader, a computer running the software, a function generator creating alternating current, and a spiral magnetic coil

generating electromagnetic field (see section 1.3.1). In order to conduct all the coil tests, a device that can simulate the electromagnetic field characteristic created by the deactivator is needed.

For the testing device, the exact same primary coil was installed in the empty housing of the deactivator. An external function generator was connected to the coil to provide power. Due to the limited power output of the function generator, this experimental apparatus could not function as a deactivator, i.e. it could not provide enough power to heat up the aluminum foil and expand the enabler. However, it could generate a field with the same frequency and shape characteristic as the deactivator. An oscilloscope is used to monitor the voltage input in the primary coil and the voltage induced in the field repeater.

5.4. Preliminary Experiments

5.4.1. Evaluation of the Apparatus

First of all, a comparison test between a working deactivator and our own experiment apparatus was performed to validate that the experimental apparatus is a good replicate of the deactivator. In this test, 6 different resonators were used, with coils of various gages and turns. These coils were manufactured in China. They are listed in Appendix E. As they were made by winding machines, the quality is consistent. Details about the variability analysis of these coils are exposed in chapter 7 and [19]. The coils were paired with specific capacitors to ensure that the natural frequencies of the field repeaters were close to 220 kHz, which is the optimal working frequency of the deactivator. The function generator was also adjusted to 220 kHz. The power output of the function generator was kept constant to -0.12 dBm. During the test, each coil was put at 1.125 inch above the center of the coil (1 inch + thickness of deactivator top cover). Voltage of the primary coil and the field repeater were both monitored using an oscilloscope. The measurement sequence was randomized, and 4 additional replicates were collected to minimized measurement error. The data collected from each test were analyzed with *Minitab*.
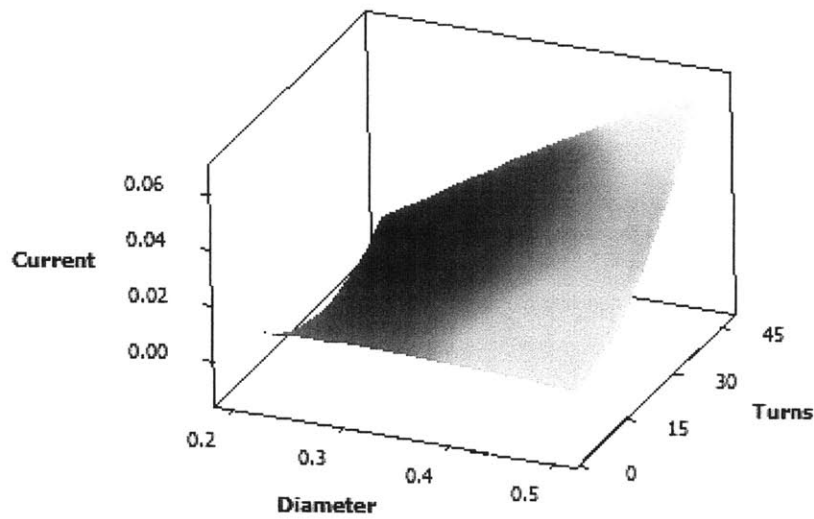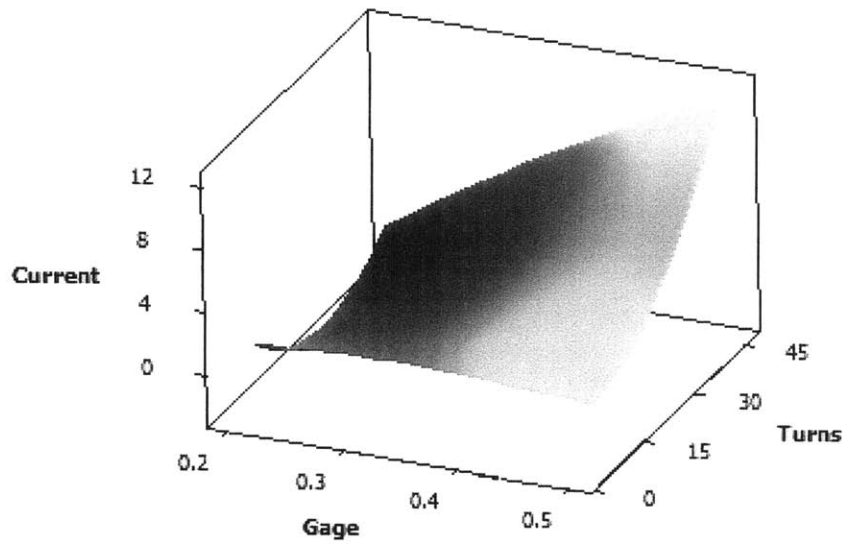
Figure 14: Response surface comparison for tests run on a working deactivator (left) and tests run on the experimental apparatus (right)

Because the power outputs of the deactivator and the experiment apparatus are different, the values of current do not have the same order of magnitude. However, the shapes of the surfaces are almost identical. Thus, results from the experimental apparatus are entirely transposable to the current tablet used at ProTeqt.

5.4.2. Experimental Output

For all the experiments, the only recorded outputs were the input voltage in the primary coil and the voltage in the secondary coil. It was expected that the higher the induced voltage, the more efficient the coil. Thus, we came with the following classification of the coils from our manufacturer:

Table 1: Maximum Voltage for the 6 different coils

Rk.	Coil	Natural Frequency	Maximum Voltage in the Coil
1	#6 – 47 turns, AWG 32	190 kHz	3.42 V
2	#1 – 9 turns, AWG 24	214 kHz	2.10 V
3	#2 – 9 turns, AWG 28	215 kHz	2.08 V
4	#5 – 16 turns, AWG 28	209 kHz	1.96 V
5	#4 – 6 turns, AWG 24	239 kHz	0.80 V
6	#3 – 9 turns, AWG 32	223 kHz	0.65 V

In Table 1, the voltage in each coil has been measured at the natural frequency. The highest voltage is achieved with coil #6, far ahead of the other ones. However, when it came to test these coils on an actual deactivator to expand an enabler, the coil #6 failed all the time whereas coils #1 and #2 worked reliably. As a result, induced voltage does not seem to be a good indicator of coil efficiency.

As seen on section 4.2, what makes a coil efficient is the amplitude of the magnetic field it can generate to heat up the enabler. The magnetic field is proportional to the current across the coil. Thus induced current is actually a better indicator of the coil efficiency.

The way to determine current in the secondary circuit is fully explained in appendix C, but the resulting expressions is

$$I_{RMS} = \frac{V_{pp}/2\sqrt{2}}{\sqrt{R^2 + (2\pi f L)^2}} \tag{5.1}$$

Thus, using this equation, the classification of the coils is changed as follows:

Table 2: Maximum Induced Current through the secondary circuit

Rk.	Coil	Natural Frequency	Maximum Current in the Coil
1	#1 – 9 turns, AWG 24	214 kHz	0.86 A
1	#2 – 9 turns, AWG 28	215 kHz	0.86 A
3	#4 – 6 turns, AWG 24	239 kHz	0.83 A
4	#5 – 16 turns, AWG 28	209 kHz	0.29 A
5	#3 – 9 turns, AWG 32	223 kHz	0.27 A
6	#6 – 47 turns, AWG 32	190 kHz	0.062 A

In Table 2, we see that even though the coil #6 exhibited the highest voltage, it generates the smallest current. Indeed, the inductance is the predominant term in eq. (5.1) and it is one order of magnitude higher for coil #6. On the other hand, the two most reliable coils (#1 and #2) generate the highest level of current. This new ranking is totally consistent with enabler expansion test on the real deactivator.

5.4.3. Distance Effect on Natural Frequency

For preliminary tests, the secondary coil has been tested at various distances from the primary one. It appeared that the natural frequency of the system increases with distance. More precisely, it tends asymptotically to a frequency that is slightly smaller than the natural frequency of the LC circuit. As a reminder, the natural frequency of an LC circuit is given by the following relationship:

$$f_0 = \frac{1}{2\pi\sqrt{LC}}$$
(5.2)

This is confirmed by the test results, on Figure 15. The tests have been done with coil #1 (9-turn coil with AWG 24) and capacitor of $1\mu F$. The natural frequency of this circuit is 214 kHz.
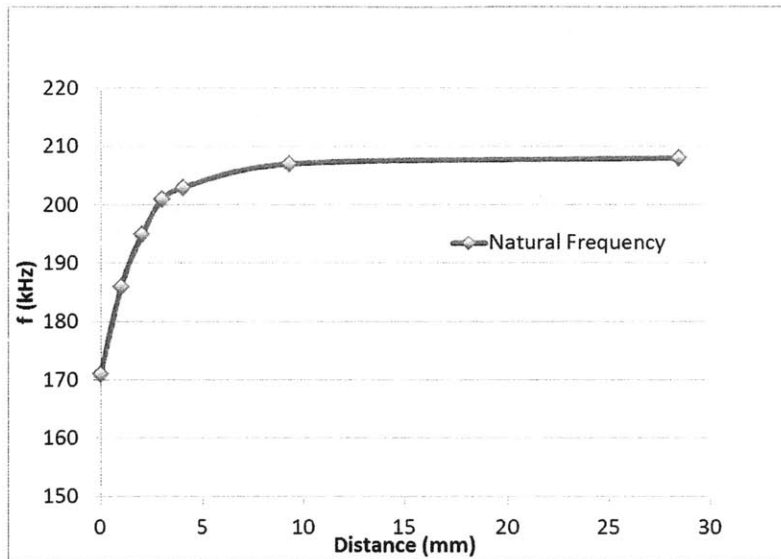
Figure 15: Natural frequency of the system versus the distance between the two antennas

Understanding this frequency shift is crucial in the design phase. Indeed, the objective is to tune each LC circuit to a certain natural frequency. This frequency is determined by the values of inductance and conductance, as shown in equation (5.2). If the two antennas (primary and secondary coils) are close, the natural frequency of the secondary circuit must be tuned higher than the frequency used to open the lock. For our application, the distance between the two coils is one inch. The frequency shift remains reasonably low and is mostly compensated by another cause of frequency shift: the presence of the enabler (see section 5.6.2).

5.5. Experimental Characterization of the Design

5.5.1. Response surface of the Current

To verify the theoretical model response surface derived in section 4.2, LC circuits were made with 6 different antennas. Each circuit is tuned to have its natural frequency around 220 kHz.

Table 3: List of LC circuits for experimental current response surface

Coil	Capacitance	Natural Frequency
#1 – 9 turns, AWG 24	$1\ \mu F$	214 kHz
#2 – 9 turns, AWG 28	$1\ \mu F$	215 kHz
#3 – 9 turns, AWG 32	$1\ \mu F$	223 kHz

47

#4 – 6 turns, AWG 24	$2 \, \mu F$	239 kHz
#5 – 16 turns, AWG 28	$0.43 \, \mu F$	209 kHz
#6 – 47 turns, AWG 32	$0.055 \, \mu F$	190 kHz

The voltage in the inductor is measured in order to get the maximum induced current (see section 5.4.2). Five replicates have been taken for each circuit. From these data, a response surface has been designed with two factors: (a) the gage size and (b) the number of turns.

5.5.2. Efficiency of the Coupling

As explained in chapter 2, the secondary LC circuit acts as a pass-band filter. It resonates at a specific range of frequencies, whereas there is almost no power transfer at low and high frequencies. To show this property, it is possible to plot experimentally the transfer function of the system. For that, the same experimental apparatus is used (see section 5.3). After the resonant frequency has been found, the input frequency is set to its lowest possible value. To get readable voltage input and output, we usually started at 115 kHz. Then, the input frequency is progressively increased until the highest readable value (most often, around 400 or 500 kHz). At each measuring point, the operator records the frequency, the peak-to-peak voltage through the primary coil and the peak-to-peak voltage through the secondary coil. To get an accurate plot, the measurements are refined around the resonant peak. Considering the measurement precision, it is unnecessary to decrease the resolution below 1 kHz.

As demonstrated earlier in the chapter (section 5.4.2), the efficiency of a coil relies on its ability to generate a high current. Thus, the plots are more meaningful if the input and output are the current through the primary and secondary circuits respectively. Figure 16 shows a typical plot.
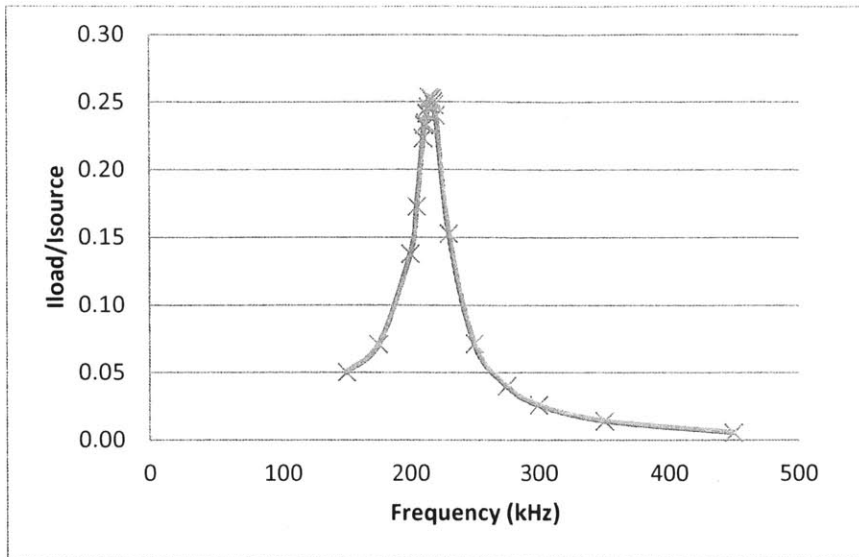
Figure 16: Transfer Function Plot for Coil #1 (9 turns, AWG 24, 1μF capacitance)

Figure 16 shows each individual data point. For maximal accuracy, the number of points was largely increased around the resonant frequency. Due to the measurement method (oscilloscope), the voltage is given with a precision of

- $\pm 10 \ mV$ for the peak-to-peak voltage in the primary coil, and
- $\pm 0.1 \ mV$ for the peak-to-peak voltage in the secondary coil.

An efficient coil would exhibit a high and narrow resonant peak. High peak means high energy transfer efficiency at resonant frequency. Narrow peak means high frequency selectivity, i.e. the enabler can be activated by a short range of frequencies only.

These experimental plots are used to point out the phenomena that can affect the quality of the coupling, besides the distance between the two antennas. For effect of distance, one can refer to section 5.4.3 and appendix D. The following elements have been explored:

- The other components of the lock, especially the enabler
- The size of the enabler

5.6. Optimization Results

5.6.1. Optimal Secondary Coil

First of all, we plot the response surface in current for the six tested LC circuit:
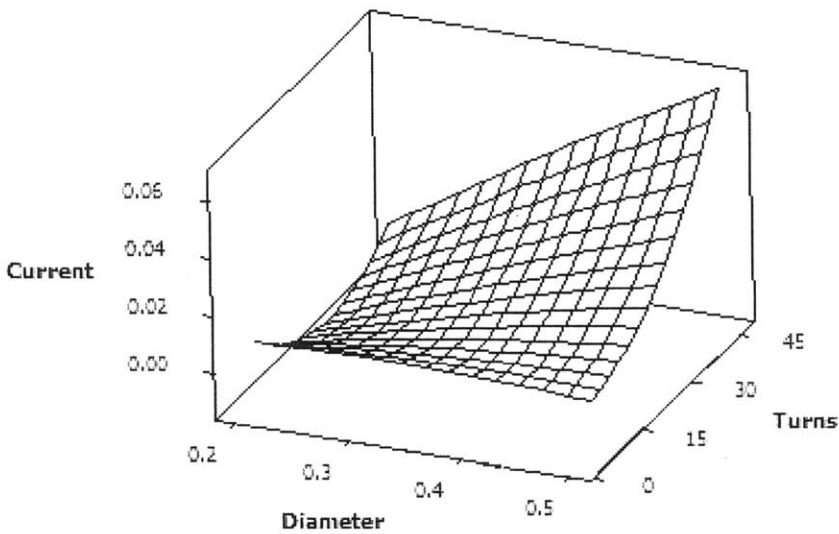
Figure 17: Response surface in current for various coil characteristics.

The regression of the data point has an R-square of 99.71%.

Before choosing the ideal coil according to the theoretical analysis (section 4.2), it is first necessary to validate the model. For that purpose, the current surface is compared to the experimental response surface for current that was designed with the six different coils.
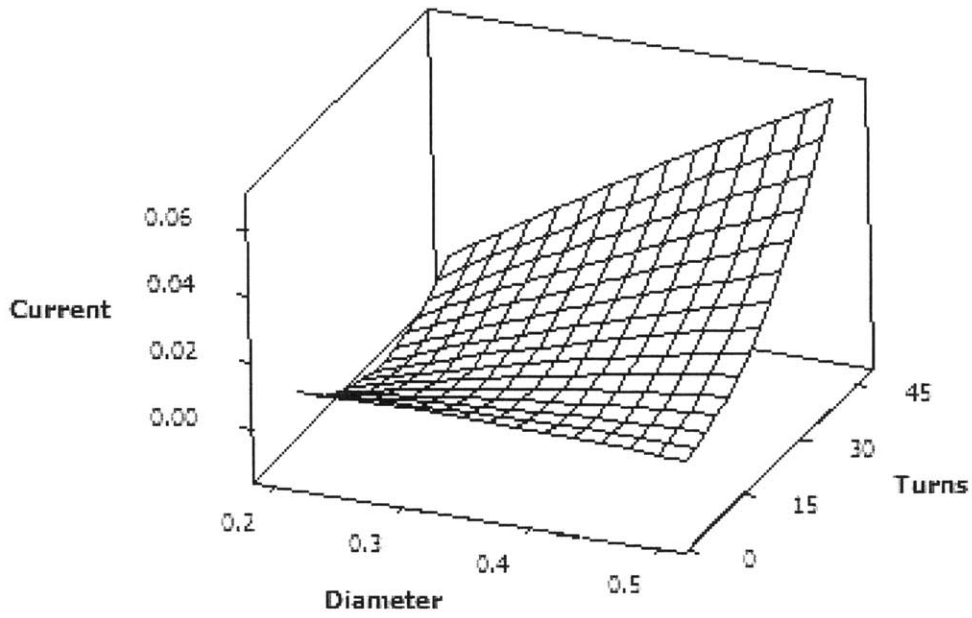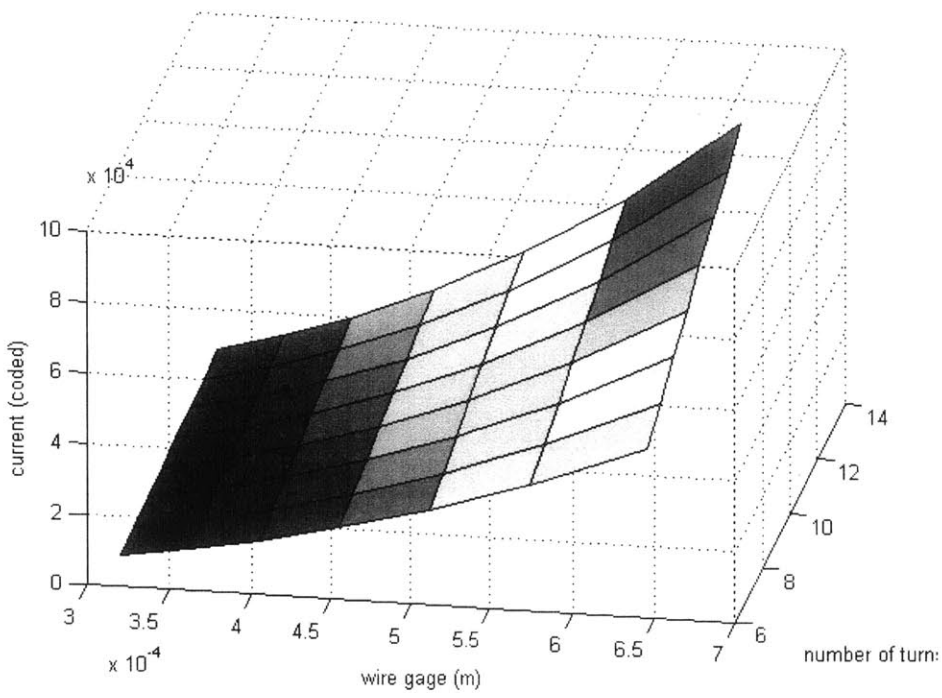
Figure 18: Induced current in secondary coil versus wire gage and number of turns. Theoretical model (left) and experimental response surface (right).

51

Figure 18 exhibits the exact same trends between the theoretical model and the experimental response surface. In particular, both approaches show that induced current increases with the number of turns and the gage size. Ultimately, we want to maximize both parameters. However, the size of the coil is geometrically constrained (see introduction of this chapter). Indeed, the gage size must not exceed AWG 24 (0.551 mm) and the outside diameter must be lower than 12.74 mm. Table 4 shows the theoretical values of induced current (coded unit) for coils with various gage sizes and number of turns. Data are from the model presented in section 4.2. From this table, the gray cells correspond to coils that exceed the geometric specifications of the lock. Among the remaining cells, we select the coil that provides the highest current. Theoretically, the coil that provides best result should be a coil with 9 turns and a gage size of 24 (0.551 mm). If needed, two other coils could be considered with slight modifications on the lock design: a 9-turn with gage 23 and a 10- turn with gage 24.

Table 4: Current (coded unit) versus number of turns and gage size

Turns AWG	6	7	8	9	10	11	12	13
22	4.76	5.29	5.82	6.36	6.90	7.45	7.99	8.54
23	3.56	3.94	4.31	4.69	5.07	5.45	5.83	6.21
24	2.68	2.94	3.20	3.47	3.73	4.00	4.27	4.54
25	2.03	2.21	2.39	2.58	2.76	2.95	3.14	3.33
26	1.53	1.66	1.78	1.91	2.04	2.17	2.30	2.43
27	1.17	1.26	1.35	1.44	1.54	1.63	1.72	1.81
28	0.89	0.95	1.01	1.07	1.14	1.20	1.27	1.33

This theoretical result is supported by experiments. Among the six coils that were tested, the one that provide highest current is the 9-turn coil with AWG 24 (see Table 2, page 46).

The current values for the experimental response surface are significantly smaller than the ones we observed during the preliminary tests. As the function generator is a basic model, it is difficult to set it up to the exact same input voltage from one day to another. However, for each series of experiments, all the data have been taken with the exact same set up.

5.6.2. Effect of Enabler on the Resonant Frequency and the Coupling Quality

After being tested alone, one of the LC circuits was inserted inside a functioning lock. The current gain is plotted in Figure 19. Adding the lock elements has two effects: (a) it dampens the peak by 80%, and (b) it increases the resonant frequency by around 10 kHz.
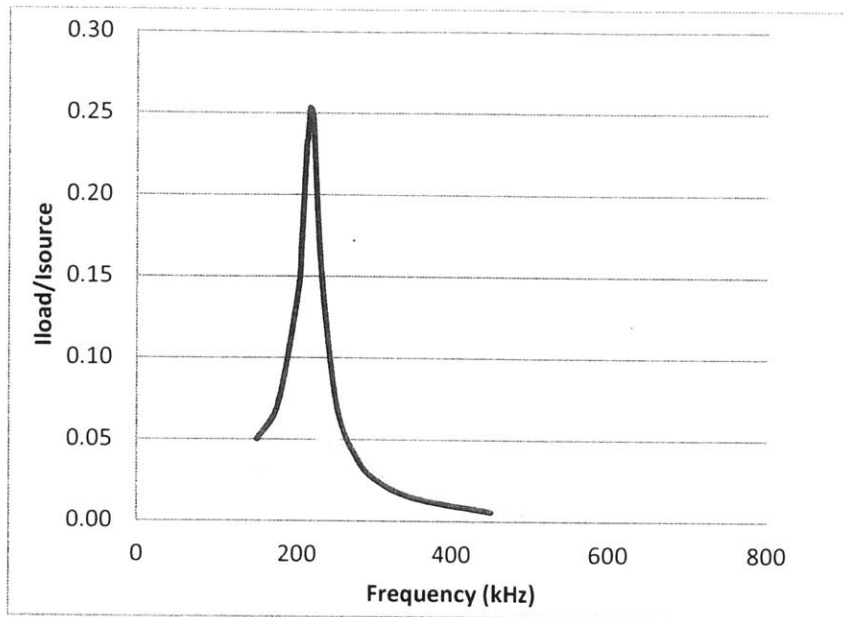
Figure 19: Efficiency Plot in current of coil #1 (9-turn and AWG 24) with (grey) and without (black) the entire lock

The reason for this is the presence of metal pieces around the coil (enabler, spring and sheet metal). These pieces have been tested separately to exhibit their respective effect on the coupling efficiency. The entire effect seems to come from the enabler, which is a layer of epoxy in between two aluminum foils. The size of the enabler is a rectangle of 9mm by 12mm. The other metal parts effect is too low to be measured on this oscilloscope.

The effect of the enabler on the resonant frequency is not problematic as long as the shift is known. Indeed, the natural frequency of the secondary circuit can be easily tuned in order to compensate for it. However, the dampening effect is hardly impossible to compensate without reconsidering the entire design. Thus, this effect must be minimized. The most direct way consists of reducing the amount of metal around the LC circuit. For that purpose, some tests have been conducted with only half of the enabler, i.e. a rectangle of 9mm by 6mm.

53
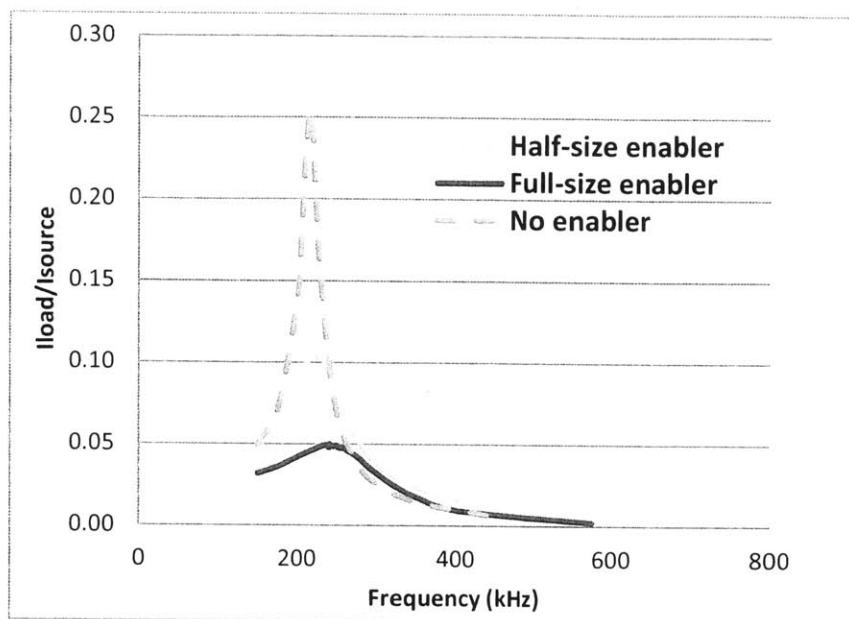
Figure 20: Efficiency Plot in current for coil #1 (9 turn and AWG 24). Without enabler (dash), with half of an enabler (grey) and a full enabler (black)

Figure 20 shows the efficiency plot of a coil with half of an enabler. The curve is intermediate between the two initial plots (Figure 19, reused in Figure 20). For this coil, the enabler dampens the efficiency by 55% and shifts the resonant frequency by 5 kHz. This strategy seems to be efficient to reduce the dampening effect of the enabler on the coupling efficiency. However, two questions remain at this point:

1. Is the coupling efficiency sufficient and provide enough energy to expand an half sized enabler?
2. Then, can half sized enabler provide enough force to open the lock in the current design?

The answer to the first question is yes. Tests on the optimized coil with half sized enabler were conducted on the real deactivator, at full power. Each time, the enabler received enough energy to expand up to a distance of 1.5 inch between the primary and secondary coils.

The second question is analyzed in chapter 6. More detail can be found in [20].

5.7.   Other Coil Designs

Depending on the technology available and the allocated budget, other coil designs could be explored.

5.7.1. The Case of Litz Wire Coil

To improve even more the efficiency of the coil, litz wire can be used instead of simple copper wire. It consists of many thin wires, individual insulated and twisted together. This kind of wire is extremely useful for AC current application because it allows reducing the skin effect. It is expected to significantly increase the efficiency of the energy transfer between the primary and secondary coils. One test has been done with a 6-turn coil made of 20/34[5] litz wire.
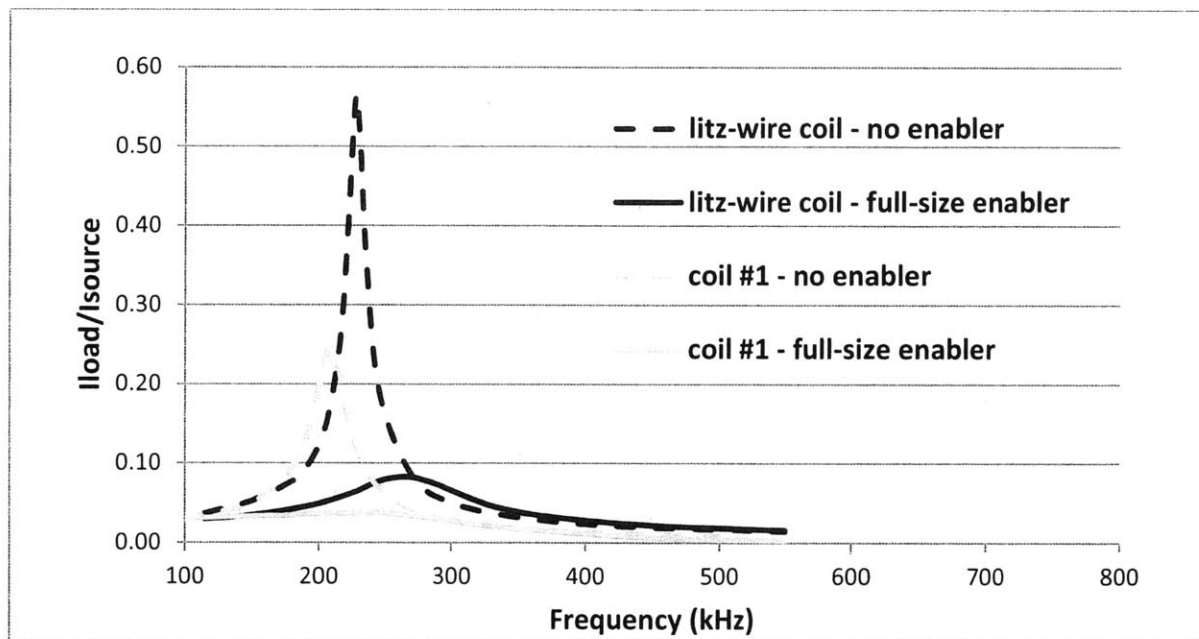
Figure 21: Efficiency Plot in current. Comparison between litz wire coil and 9-turn AWG 24 coil (#1). Without enabler and with full-size enabler

Figure 21 shows that litz-wire coil exhibit a much better efficiency, compared to our optimized copper wire coil. However, the comparison should be considered with caution because the litz-wire coil is also larger. If ProTeqt would go in this direction, further analysis (theoretical and experimental) should be done. We do not encourage this kind of solution for the locks that are 1 inch away from the tablet, because it would be significantly costlier.

---

[5] 20/34 is the gage of the litz wire. 34 is the AWG of each inner wire and 20 is the gage of the whole wire.

5.7.2. The Case of Thin Wire Coil

All the previous analysis has been conducted with winding copper coils. They are indeed easy to make in small quantity and very flexible. However, we may want to consider other manufacturing methods for full-size production, especially etching or inkjet. Beside their costs, with these methods, only coil with a very thin copper layer can be produce. As a consequence, their resistance will be significantly higher. As shown previously (see section 5.4.2), in our application, efficiency of a coil is measured by the intensity of current that can be induced. Thus, it is important to achieve low resistance. So, the actual optimized design has to be reviewed for the case of thin wires.

In order to decrease the resistance of the coil, we propose a new design, inspired by the litz-wire solution. The printed coil consists of three parallel lines in spiral (see Figure 22 right). In order to get a coil with the same size as the regular design, the new design has only three full turns.
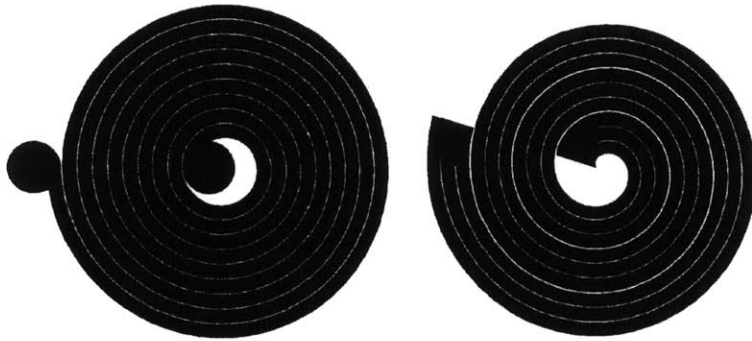
Figure 22: Regular coil design (left) and thin wire coil design (right)

This design is expected to significantly decrease the resistance of the coil. However, further tests have to be conducted to verify if this design effectively increases the magnitude of the secondary magnetic field.

Chapter 6

Mechanical Lock Analysis

6.1. Objective

The success of ProTeqt requires the force generated by the enabler to be greater than the force required to disengage the mechanical system. The objective of the analysis on the mechanical lock can be separated into two parts. First understand the forces required to disengage the lock should be understood (section 6.3), followed by the forces that can be achieved by the enabler at a distance of zero and one inch (section 6.1).

This chapter is a summary of the entire lock analysis, which was done in ProTeqt during the internship. For full detail about it, one can refer to [20].

6.2. Introduction to the Mechanical Lock

Figure 23 shows the internal mechanism of the lock. For protection of trade secret, the real shapes of the parts are not shown. All these parts are encapsulated inside a plastic body. The lock is attached to the micro-USB port through the teeth of the sheet metal 1 (right end of the sheet metal 2). The entire locking system relies on the contact surfaces between sheet metal 1 and 2. Especially, there is a vertical frictional contact surface between these two components (hidden by the left end of metal sheet 2, on Figure 23). At the deactivation, when the enabler expands, the plastic component is pushed up and bends the sheet metal 1. Thus, sheet metal 1 and 2 lose their vertical contact surface. The spring pushes the sheet metal 1 horizontally through the sheath (sheet metal 2). This displacement releases the teeth from the micro-USB port.
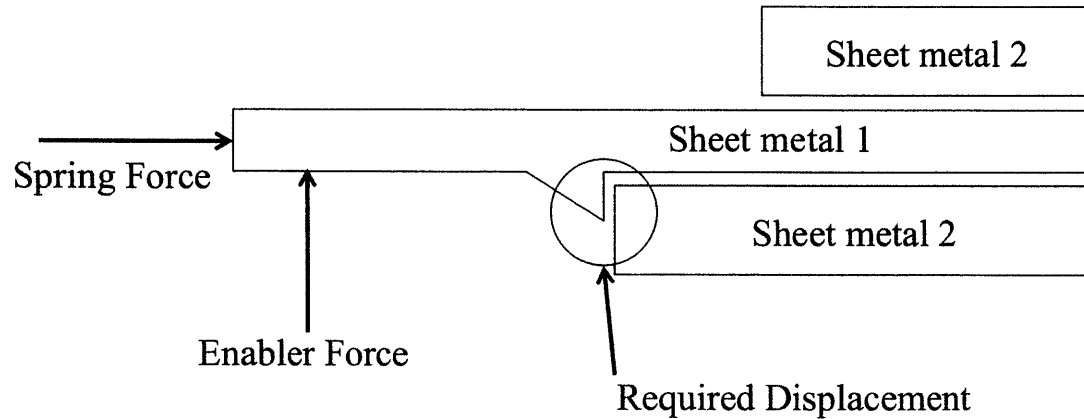
Figure 23: Schematic of internal mechanism of the micro-USB lock, developed by ProTeqt

6.3.   Mechanism Analysis

To have an idea of the force required to open the lock, three analyses were completed: (a) analytical calculations, (b) a finite element analysis (FEA), and (c) empirical tests.

6.3.1. Analytical Calculations

Considering the constraint of the sheet metal inside the sheath, the portion of it that bend is considered as a cantilever beam. The force required is divided into two components: (a) the bending force and (b) the friction force. All equations and assumptions are detailed in Appendix F.

Bending force

According to the CAD files, the sheet metal must move up by 0.434 mm at the contact surface with the sheath. So, the theoretical bending force required is $F_{bending} = 17.7\ N$. As this is much higher than the force we got from preliminary tests, we tried to estimate the play between the parts. If now, the bending displacement is reduced to 0.1 mm, the theoretical bending force is $F_{bending} = 4.07\ N$.

Friction force

Using the theory of Coulomb friction, we assume a kinetic friction coefficient $\mu = 0.8$. Given the spring constant of the spring $k = 525\ N/m$, the theoretical force required to overcome friction is

$$F_{friction} = 6.94\ N$$

To conclude, this theoretical analysis predicts that the required force to open the lock is

$$F = 11.01 \, N$$

6.3.2. Finite Element Analysis (FEA)

This analysis was conducted with the FEA package of *SolidWorks*. The sheet metal 1 was insulated and loaded as show on Figure 24. As it was not possible to control the displacement, different force values were tried. To get a displacement of around 0.4 mm, the force must be 15N. Then, for a displacement of 0.1 mm, 4N is sufficient.
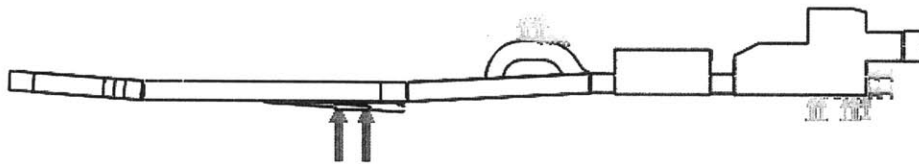
Figure 24: Constraints and load applied in the FEA. Small arrows are for completely fixed surfaces. Long arrows are for force from the enabler.

Considering that this FEA does not include the friction force, the results are consistent with the theoretical model.

The main drawback of these two previous methods (FEA and analytical model) is their strong assumptions on the boundary conditions. Indeed, each time, the sheath around the sheet metal 1 was assumed to be rigid. This hypothesis is too strong since both parts are made of the exact same material and manufacturing process. As a result, the force required to open the lock is actually expected to be experimentally lower. Eventually, these initial results may be seen as upper bound of the real required force.

6.3.3. Empirical Tests

In ordinary operation the user, or customer, does not have access to the internal components of the lock. For the purpose of testing, one side of the external housing was removed, leaving the internal components exposed. The plastic hinge, LC circuit, and enabler were removed for testing. This allowed enough space to access the sheet metal components using a probe fastened the end of a force gage. The spring remained inside the lock throughout testing to provide results that were simulated by the analytical calculations. The empirical measurements are a sum of the forces due to friction and bending.

$n = 30$ data points were taken. The distribution is close to normality, with a mean of 1.844N and a standard deviation of 0.3048N. As expected, the experimental disengagement force is much lower than the forces calculated before. As seen in section 6.3.2, this force was previously overestimated because of too strong assumptions about the boundary conditions.

As only one lock was used, the variance of the data is solely due to measurement error. In order to minimize this error, we consider the distribution of the sample mean. It is assumed to be normally distributed with a mean $\mu_{\overline{X}} = 1.84\,N$ and a standard deviation $\sigma_{\overline{X}} = s/n = 5.5 \times 10^{-2}\,N$. The two distributions are plot on Figure 25.
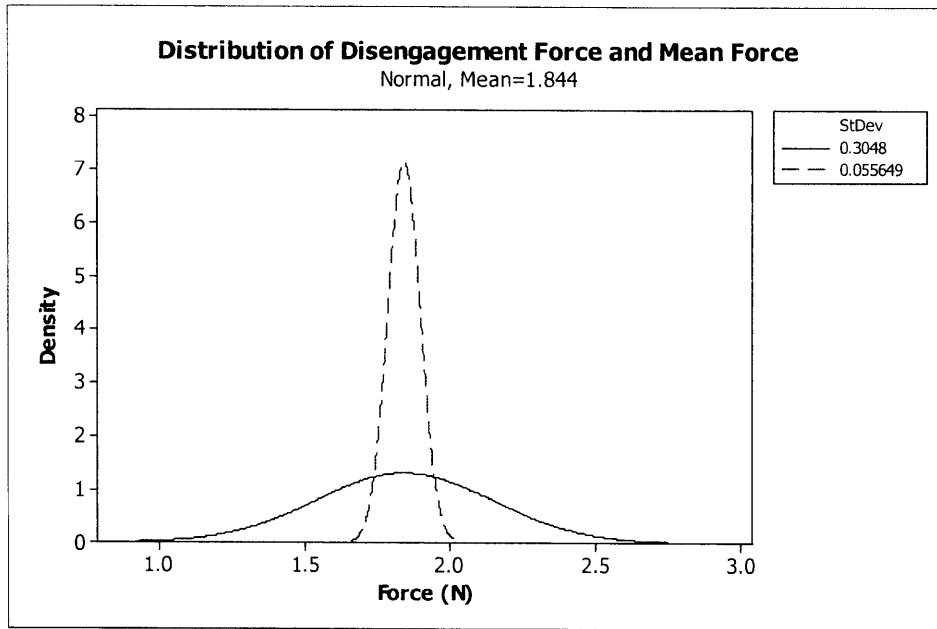
Figure 25: Disengagement force (solid) and mean force (dash) distributions

The mean and the standard deviation of the mean force are only estimates. The 90% confidence intervals (using a t-distribution since both mean a variance are estimated from a small number of samples) of these values are

$$\mu_{\overline{X}} \in 1.844 \pm t_{\alpha/2,n-1} \cdot \frac{s}{\sqrt{n}} = [1.75\,;\, 1.94] \tag{6.1}$$

$$\sigma_{\overline{X}} \in \left[\frac{(n-1)s^2}{\chi^2_{1-\alpha/2,n-1}} \cdot \frac{1}{\sqrt{n}}\,;\, \frac{(n-1)s^2}{\chi^2_{\alpha/2,n-1}} \cdot \frac{1}{\sqrt{n}} \right] = [3.79\,;\,9.11] \times 10^{-2} \tag{6.2}$$

where $t_{\alpha/2,n-1}$ is the $\alpha/2$ upper percentage point of the t distribution with $n-1$ degrees of freedom, $\chi^2_{\alpha/2,n-1}$ is the $\alpha/2$ upper percentage point of the χ^2 distribution with $n-1$ degrees of freedom and n is the sample size.

6.1.   Enabler Force Analysis

6.1.1. Objectives

Understanding the force required to disengage the lock is very useful, in that the enabler can now be designed to a certain level of robustness. That is, the enabler can be designed to interact in a way that it produces a certain force. This force can be compared to the force required to disengage the lock. If the force produced by the enabler does not exceed the force required by the lock, it will fail to disengage.

Experiments were conducted to gain a better perspective of the forces produced by the enabler. Several parameters are considered:

- Size of the enabler,
- Level of vertical and lateral confinement of the enabler, and
- Interaction between the enabler and the LC circuit.

6.1.2. Experimental Apparatus

The experimental apparatus was designed to be accurately representative of the real use, inside the lock housing. However, it was also kept as flexible as possible, in order to easily vary the parameters of interest. A diagram of the apparatus is drawn in Figure 26. In order to measure the force provided by the enabler, a force gage was attached to a rigid frame, above the enabler. For lateral confinement, the enabler was placed in a pocket of known size, laser cut in a piece of Lexan. An example of this fixture is given in Figure 27. To protect the gage from the enabler expansion, another piece of Lexan is placed on top of the first one. For good vertical confinement, pieces of cardboard were inserted in the pocket. The vertical constraint is modified by changing the number of cardboard pieces (zero, one or two).
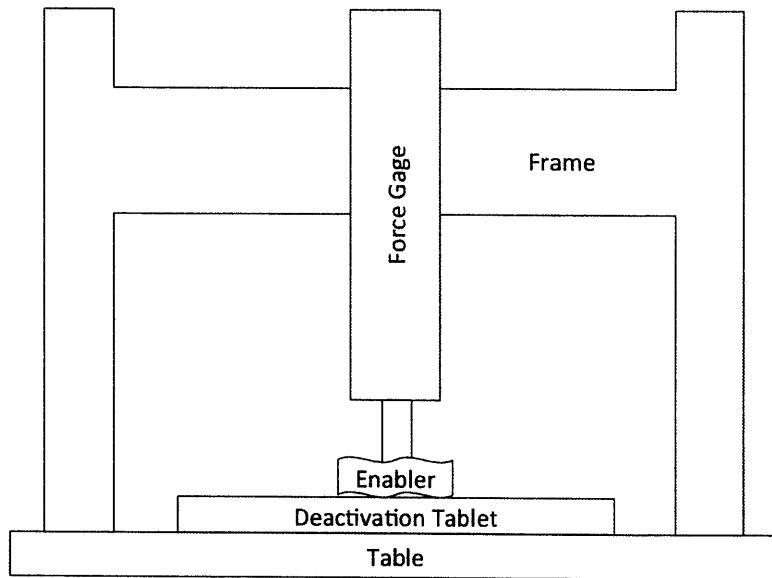
Figure 26: Functional diagram of the experimental apparatus
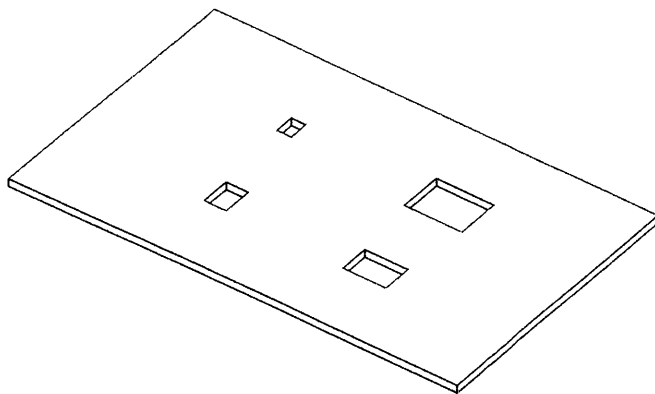
Figure 27: Model of an enabler constraint fixture.

6.1.3. Data Collection

First an analysis of the effects of deactivation time, or time that the deactivation tablet produced the desired field, were conducted to find the optimal time to run all proceeding experiments. With a fixed time, the effects of constraining the enabler both vertically and laterally were analyzed to predict performance within the lock, given certain dimensional constraints and tolerances inherent in the manufacturing processes. With an understanding of the constraining effects, tests of the full enabler were run on the tablet and at one inch above, using the LC circuit. Finally, tests were conducted to understand the effects of using a half sized enabler, as recommended to increase the coupling efficiency between the primary coil and the LC circuit.

Optimal Processing Time

Disengagement of the lock should require less than one second of power from the deactivation tablet. This constraint has been set as per request from ProTeqt's potential customers. To understand the effect of deactivation time on force, five samples were taken at intervals of 0.1 second from 0.1 to 0.5 second. The deactivation time is define as the time during which an alternating current is sent to the primary coil. For full sized enabler directly on the table, data are plotted on Figure 28.
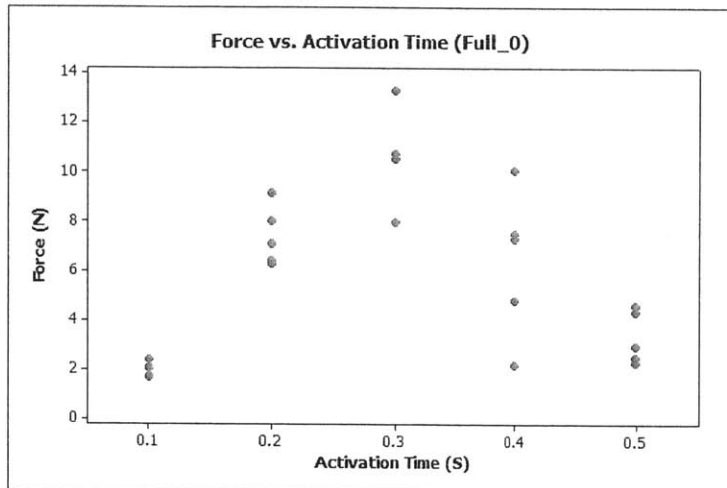
Figure 28: Individual value plot of force vs. activation time using a full enabler on the deactivation tablet

A peak of force appears around 0.3 sec. This comes with much higher variability than shorter time slots. After the peak, the enabler is burnt, preventing it to expand properly. As a result, it achieves lower force. The variability remains high, certainly because the burning process is extremely random. From these tests, we realized that the tablet should not send too much energy in a very short time slot. Indeed, the enabler requires some time to expand. So, if its temperature increases too quickly, it burns before full expansion. This phenomenon was only exhibited for tests on the tablet. At one inch, the tablet is not able to provide enough power to burn the enabler.

From these tests, an optimal deactivation time was picked. We chose to minimize the variability, yet with a mean force high enough to open the lock consistently. Table 5 provides the optimal time for each set of experiments.

Table 5: Optimal deactivation time for each experiment

Experiment	Enabler size	Deactivation Time (s)
On tablet	Full	0.2
On tablet	Half	0.2
1in. above	Full	1
1in. above	Half	1

Confinement

Different levels of lateral and vertical confinements were tested. Table 6 gives the mean force for each level (15 data points per confinement). The force achieved by the enabler is a function of the free space inside the lock. Ideally, this confinement of the enabler should be maximal. However, it must be sufficient to move the locking mechanism by 0.434mm up.

Table 6: Average force for different levels of confinement (full sized enabler, on the tablet)

		Vertical Confinement (layers of cardboard)	
		1 layer (0.43mm)	2 layers (0.86mm)
Lateral	Nominal cut	6.2N	11.1N
Confinement	1 mm of clearance	N/A	6.1N

Size of the enabler

Thirty data points were taken for half and full sized enabler, on tablet. 5 data points were taken for each test at one inch above the tablet. The confinement is maximal (nominal cut and 2 layers of cardboard). The results are assumed to be normal.

On the tablet, the full sized enabler provides more force than the half sized, with at least 90% confidence (see Table 7). This is understandable because the surface of contact with the gage is twice as large for the same thickness of epoxy. However, the ratio of the mean forces is not exactly two. The lack of accuracy of the measurements could be a reason.

However, at one inch above the tablet, the half sized enabler provides more force, with at least 90% confidence (see Table 7). At first thought, this result is surprising. To understand it, one must go back to

64

the LC circuit – enabler interaction (see section 5.6.2). Indeed, we showed that the enabler significantly decreases the coupling efficiency between the primary coil and the LC circuit. So, a smaller enabler allows better efficiency. As a result, a smaller enabler receives more energy from the LC circuit than a full sized enabler. Moreover, it requires less energy to expand entirely because of a smaller thermal mass. Interestingly enough, the half sized enabler performs better at 1 in above the tablet than directly on it. It is also believed to be a result of distance, heating properties of the system, and the efficiency of the resonant coupling. However, more data would be necessary to conclude with certainty.

All the results are summarized in Figure 29 and Table 7, with 90% confidence intervals (see equations 6.1 and 6.2 on page 60).
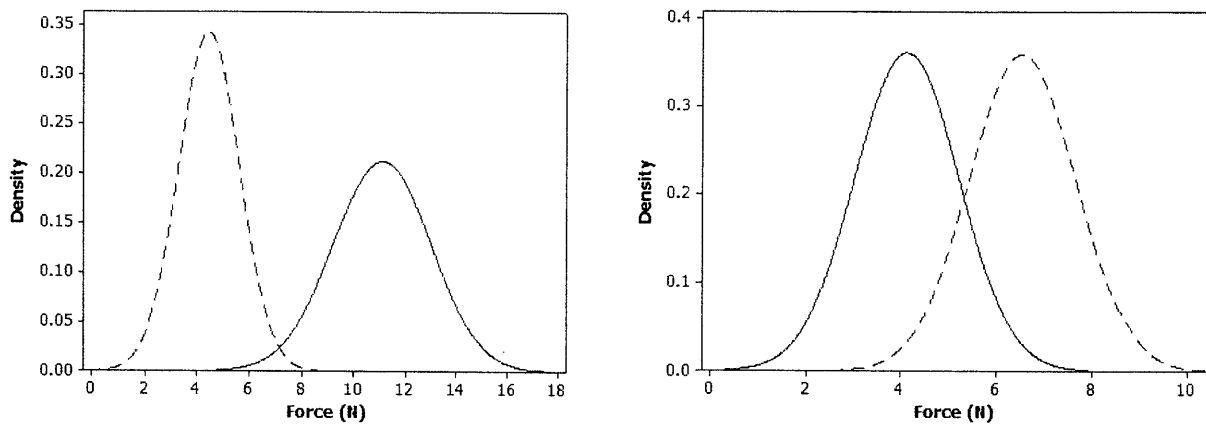
Figure 29: Force distribution for full sized enabler (solid) and half-sized enabler (dash). Right: On tablet. Left: One inch above the tablet.

Table 7: Distribution characteristics

		Mean		Std. Dev.	
		Estimate	**90%-CI**	**Estimate**	**90%-CI**
On tablet	**Full**	11.1N	[10.5 ; 11.7]	1.88N	[1.28 ; 3.08]
	Half	4.45N	[4.08 ; 4.82]	1.16N	[0.79 ; 1.90]
1 in. above	**Full**	4.12N	[3.07 ; 5.17]	1.10N	[0.46 ; 6.19]
	Half	6.56N	[5.51 ; 7.61]	1.11N	[0.47 ; 6.25]

The confidence intervals for the standard deviation at 1 in. above the tablet are wide because of the lack of data. In order to obtain better estimate of the standard deviation, a larger sample size should have been taken, but the deactivation tablet was not sufficiently available to run these extra tests.

6.2.   Lock Performance

The force distributions of the enablers are then compared to the force distribution of the lock (see Figure 30).

Distribution Plot of Force: Lock and Full Sized Enabler 1" Above Tablet
Normal
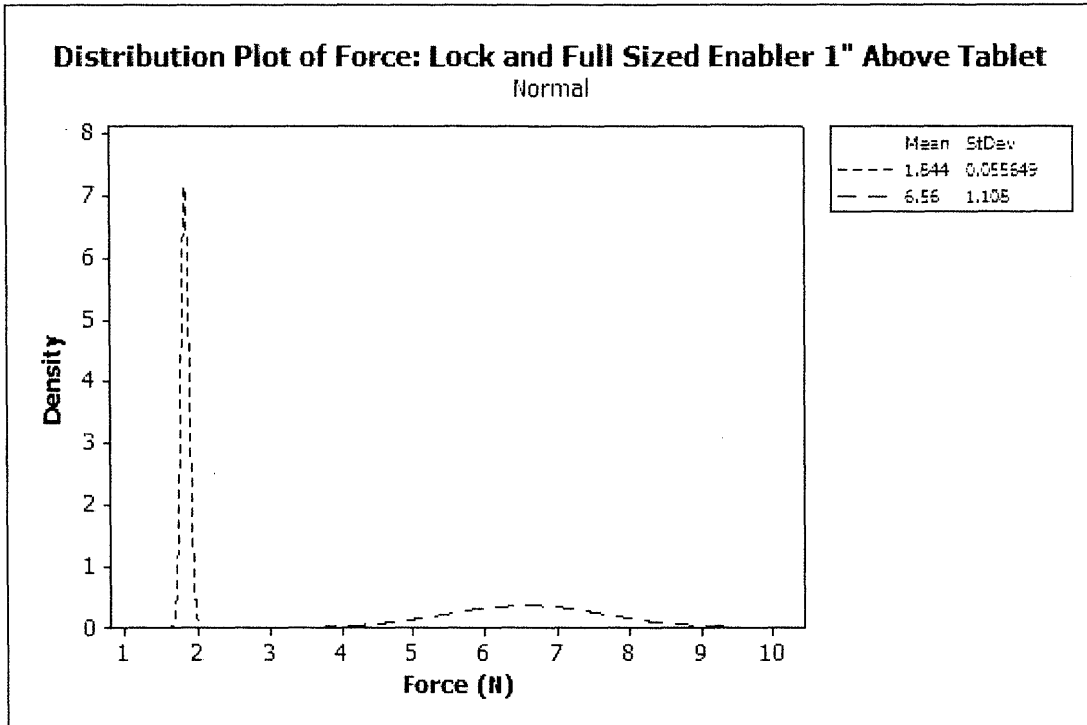
Figure 30: Force distribution. Small dash: disengagement force. Large dash: half sized enabler at 1" above the tablet.

In order to estimate the probability of failure of the lock, a new random variable Y is introduced:

$$Y = X_1 - X_2 \tag{6.3}$$

where X_1 and X_2 are respectively the force provided by the enabler and the force required to disengage the locking mechanism.

If X_1 and X_2 are assumed to be normally distributed, Y is also normally distributed with a mean $\mu_Y = \mu_{X_1} - \mu_{X_2}$ and $\sigma_Y^2 = \sigma_{X_1}^2 + \sigma_{X_2}^2$. As the standard deviation of Y is unknown, the following distribution can be defined:

$$T = \frac{Y - \mu_Y}{s_Y} \sim t(n - 1) \tag{6.4}$$

where $n = \min(n_1, n_2)$. n_1 and n_2 are respectively the sample sizes of X_1 and X_2. $t(n - 1)$ is the Student's t-distribution with $n - 1$ degrees of freedom.

Then, the probability of failure is the probability of Y to be negative:

66

$$P(Failure) = F_{t_{n-1}}\left(\frac{0 - \mu_Y}{s_Y}\right) \tag{6.5}$$

The numerical values of the probability of failure are computed in Table 8.

Table 8: Probability of failure for each of the four deactivation scenarios, with t-distribution

		μ_Y	s_Y	DoF	P(Failure)
On tablet	Full	9.26N	1.88N	29	16.2 ppm[6]
	Half	2.60N	1.16N	29	1.67×10^4 ppm
1 in. above	Full	2.28N	1.10N	4	5.39×10^4 ppm
	Half	4.72N	1.11N	4	6.57×10^3 ppm

In the chart above we see that the probability of failure is reasonably low for a full sized enabler, on the tablet. For the three other situations, the probability of failure is significantly too high for the application of interest. However, in the case of an half sized enabler at one inch above, the failure rate is one order of magnitude smaller than the full sized one. It is believed that this disappointing result come from the insufficiently large sample size for the tests conducted at one inch above. To confirm it, the limit of infinite sample size is computed. In this case, the degree of freedom of the t distribution is $+\infty$, i.e. T follows the standardized normal distribution $\mathcal{N}(0,1)$. The probability of failure becomes:

$$P(Failure) = \Phi_u\left(\frac{0 - \mu_Y}{s_Y}\right) \tag{6.6}$$

The results are given in Table 9.

Table 9: Probability of failure for each of the four deactivation scenarios, with normal distribution

		μ_Y	s_Y	P(Failure)
On tablet	Full	9.26N	1.88N	0.450 ppm
	Half	2.60N	1.16N	1.28×10^4 ppm
1 in. above	Full	2.28N	1.10N	1.95×10^4 ppm
	Half	4.72N	1.11N	10.6 ppm

---

[6] ppm : part per million

When comparing the methods, both approaches give similar results when the sample size is 30 (degrees of freedom is 29). However, the results are significantly different for a sample size of 5. Thus, further tests are expected to complete this analysis. A sample size of at least 30 would be preferable.

As a conclusion, several parameters are important to get the highest possible force from the enabler. At one inch above the tablet,

- The enabler should be smaller than the coil, and
- The processing time can be long with no risk of burning the epoxy before it expands.

On the tablet,

- The processing time should be carefully calibrated in order to prevent the enabler from burning, and
- The larger the enabler, the better.

In both cases,

- The force from the enabler increases with the volumetric constraints.

Chapter 7

Simulation of LC Circuit Variability

7.1. Objectives

The objective of this part is to understand how the manufacturing variability of the inductors and capacitors affect the force that the enabler can provide. Ultimately, this analysis would allow selecting the proper accuracy of the capacitors (typically 5%, 10% or 20%). In order to complete the entire analysis, a certain number of assumptions were made. They are highlighted all along this section. This section only highlights a limited part of the work done at ProTeqt on manufacturing variability. A more exhaustive analysis can be found in [19].

7.2. Simulation of Experimental Data

The coils and capacitors are made for a certain inductance L and capacitance C. However, due to the manufacturing variability, L and C can be seen as random variables, normally distributed. Their mean and standard deviation are respectively μ_L, μ_C, σ_L and σ_C. When a coil is paired with a capacitor, the natural frequency f_0 of this LC circuit is also a random variable. As operations on random variables are extremely complicated, this last random variable was simulated on *Matlab*.

The simulation was based on the following experimental data. A 9-turn coil with a wire gage of 0.5mm was paired with a $1\mu F$ capacitor. The coupling efficiency was measured at 1 inch above the tablet with a half sized enabler on top of it, for the largest possible range of frequencies (see section 5.5.2). Under this condition, the resonant frequency of this circuit is 220 kHz. Two more LC circuits were made with the same coil but paired with different capacitors, in order to offset the resonant frequency of these circuits. The resonant frequency of the first one was down by 5%, to 210 kHz. The second one was up by 15%, to 250 kHz. By comparing the efficiency plots of these three circuits (Figure 31), we decided to assume that the resonant frequency shift does not alter the shape of the plot.
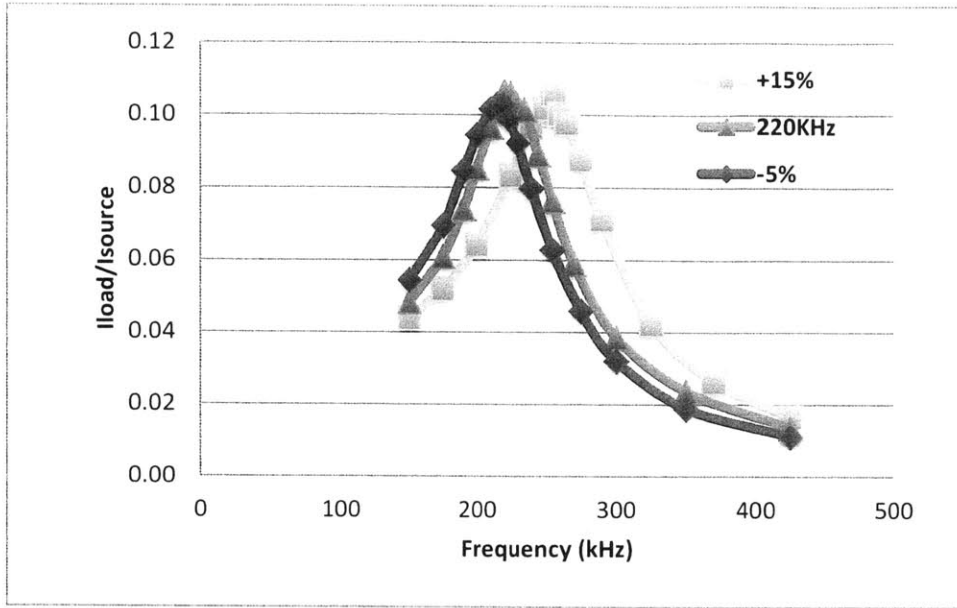
Figure 31: Comparison of efficiency plots at three different resonant frequencies: 220 kHz, 210 kHz (-5%) and 250 kHz (+15%)

Consequently it is possible to get the graph of the efficiency at 220 kHz (Eff_{220}) versus the resonant frequency (f_0) of the LC circuit. It only requires a translation of the previous efficiency plot at 220 kHz ($Eff(f)$):

$$Eff_{220}(f_0) = Eff\big(220 \ kHz - (f_0 - 220 \ kHz)\big) \qquad (7.1)$$

The strongest assumption concerns the relationship between the coupling efficiency and the force generated by the enabler. As the tablet was not available for tests at that time, we decided to implement a simple linear relationship. However, the force generated by the enabler actually depends on the temperature the epoxy reaches, with a threshold effect. If the epoxy remains below 100°C, no expansion occurs, even though there is energy transfer between the LC circuit and the enabler. Furthermore, for a given level of coupling efficiency, we assumed the force generated by the enabler to be normally distributed. This assumption takes the variability of the enabler into account. The mean and standard deviation of the force were estimated experimentally (see section 6.1 and [20]).

7.3.   Frequency Distribution

Let be the inductance L a random variable, normally distributed, of mean $\mu_L = 0.63 \ \mu H$ and with a standard deviation of 0.8%. These values were experimentally estimated with the 9-turn coils of 0.5mm

gage size, manufactured in China. The experimental determination of the inductance manufacturing variability can be found in [19]. Similarly, the capacitance C is a normally distributed random variable of mean $\mu_C = 1\mu F$. The standard deviation is determined by the quality of the capacitor. We assume the quality q given by the manufacturer is the 6σ limit. Thus, the standard deviation is:

$$\sigma_C = q\mu_C/6 \qquad (7.2)$$

The following results assume a quality of 20%. So, the standard deviation is $\sigma_C = 0.2 \times 1/6 = 0.033\mu F$.

$n_1 = 100$ realizations of each variables is generated with *Matlab*. These values are randomly paired, so we simulated n_1 LC circuits. The natural frequency of each of these circuits is defined by the following equation:

$$f_i = \frac{1}{2\pi\sqrt{L_i C_i}} \qquad (7.3)$$

Assuming the presence of an half sized enabler on the circuit, the resonant frequency is actually shift by around 19 kHz. Figure 32 shows the histogram of the resonant frequencies of these circuits, with the normal fit.
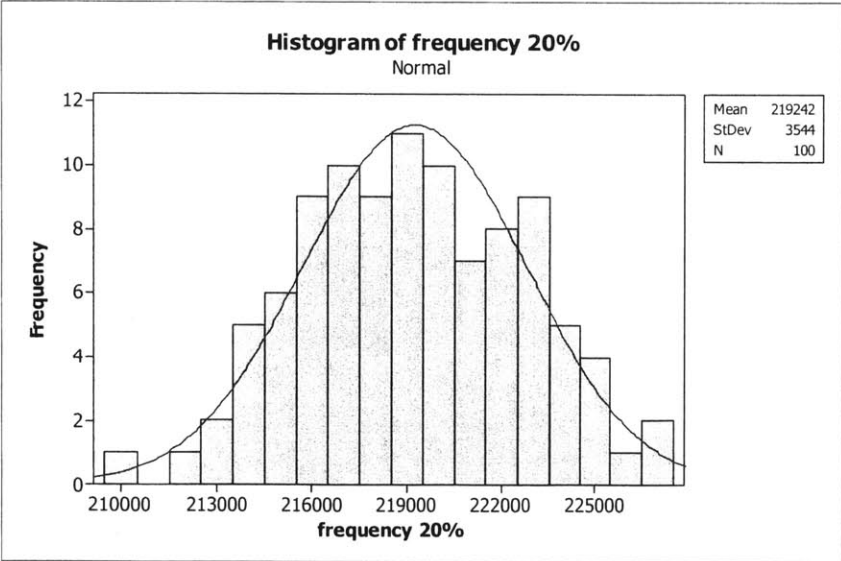
Figure 32: Histogram of the LC circuit resonant frequency

The characteristics of this histogram are summarized in Table 10

Table 10: Frequency histogram summary

Mean	219,242 Hz	Skewness	−0.0177
Standard Deviation	3,544 Hz	Kurtosis	−0.488
95% C.I. for mean		[218,539 ; 219,945]	
95% C.I. for standard deviation		[3,112 ; 4,117]	

7.4.   Fit of Efficiency Plot

A non-linear regression is conducted on the experimental efficiency plot of the LC circuit tuned to 200 kHz with half sized pillow. The plot is fitted to the following function:

$$Eff = \frac{1}{\theta_1 + \theta_2(f - \theta_3)^2} \tag{7.4}$$

This function is symmetric with respect to $f = \theta_3$. So, we lock $\theta_3 = 220 \ kHz$. The regression gives the model summarized in Table 11 and plotted in Figure 33:

Table 11: Efficiency vs. Frequency Regression Summary

Holiday Regression	
θ_1	9.70087
θ_2	$2.73731 \times 10^{-9} Hz^{-2}$
θ_3 (fixed)	$220,000 \ Hz$
Degrees of Freedom	14
Mean Square Error	2.01×10^{-5}
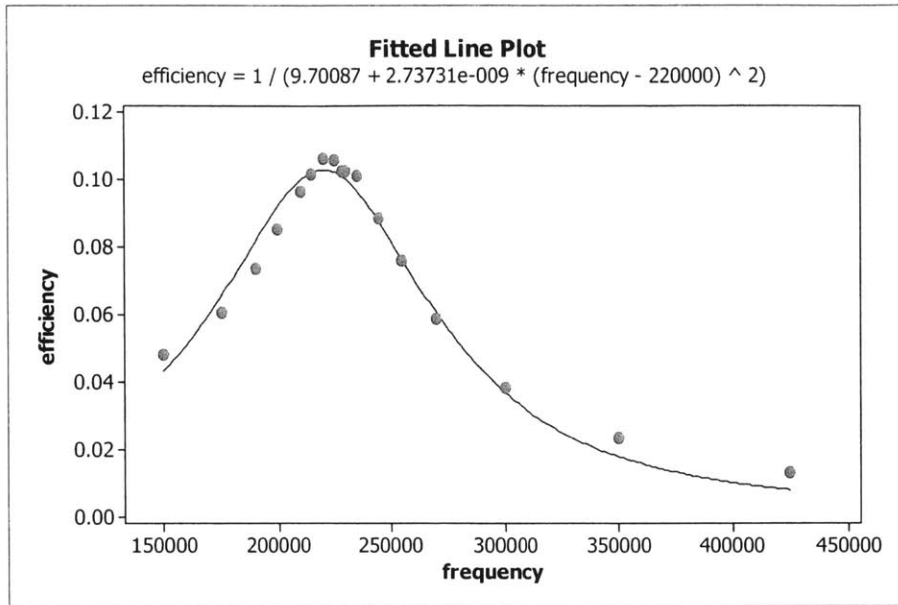
Figure 33: Plot of fit for efficiency data with respect to frequency

From eq. (7.1), the relationship between efficiency at 220 kHz and resonant frequency is

$$Eff_{220} = \frac{1}{\theta_1 + \theta_2(X - \theta_3)^2}$$ (7.5)

with $X = 220{,}000 - (f_0 - 220{,}000)$, where f_0 is the resonant frequency of the LC circuit at 1 inch above the tablet and with an half sized enabler.
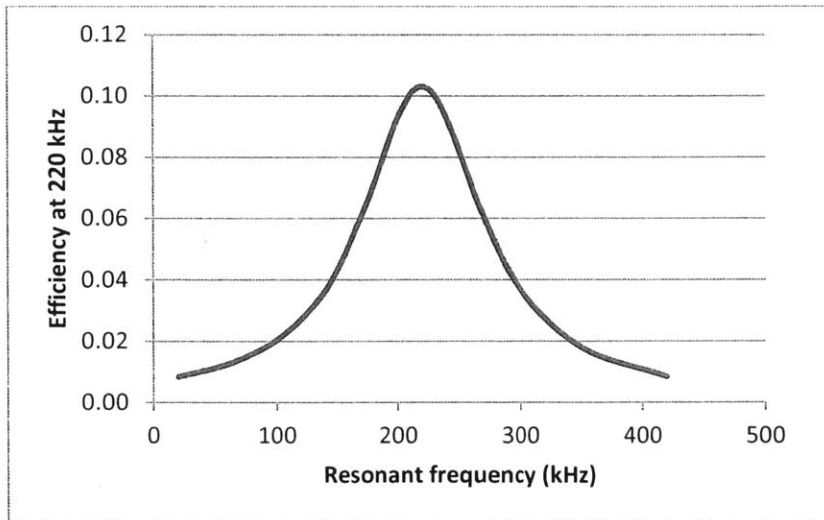
Figure 34: Efficiency at 220 kHz vs. resonant frequency of the circuit

With this relationship between efficiency at 220 kHz and resonant frequency, we can plot the histogram of the LC circuit efficiency (Figure 35).

The characteristics of this histogram are summarized in

Table 12: Efficiency histogram summary

Mean	0.10271	Skewness	-2.20
Standard Deviation	4.6×10^{-4}	Kurtosis	6.47
95% C.I. for mean		[0.10262 ; 0.10280]	
95% C.I. for standard deviation		$[4.1 \times 10^{-4} ; 5.4 \times 10^{-4}]$	
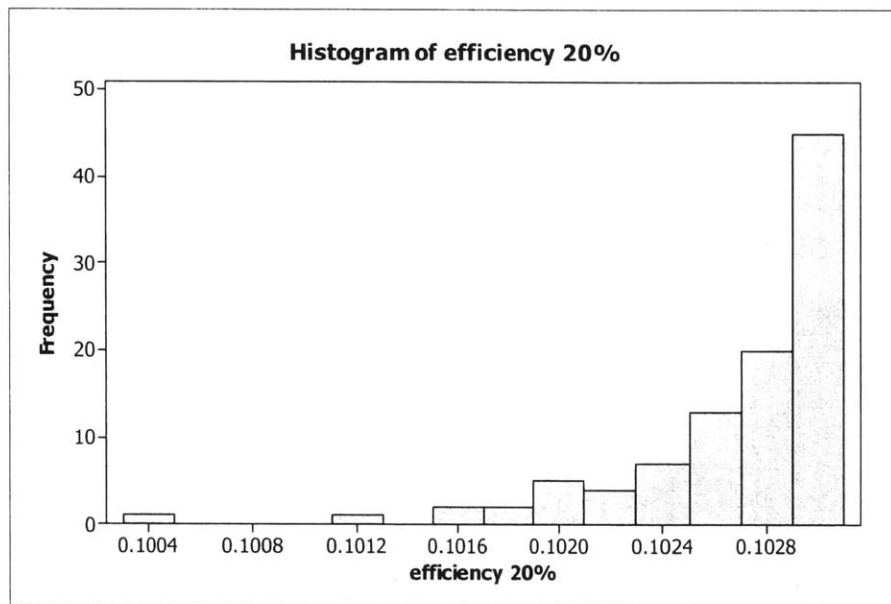
Figure 35: Histogram of the LC circuit efficiency at 220 kHz

This time, the distribution is far from normal. There is a long left tail. Indeed, the mean resonant frequency is tuned to achieve the highest coupling efficiency. Thus, if the actual resonant frequency of the LC circuit is either slightly higher or lower, the associated efficiency is always lower.

7.5. Force Distribution

Because of the lack of data, we have to assume a relationship between the coupling efficiency and the average force generated by the enabler. As a first-order approximation, we assume this relationship to

be linear. Let be F_{mean} the average force the enabler generates for a given coupling efficiency. F_{mean} is given by

$$F_{mean} = \frac{F_{mean}^{max}}{Eff^{max}} Eff \qquad (7.6)$$

with $F_{mean}^{max} = 6.56\ N$ the average force generated by an half sized enabler at 1 inch above the tablet, and $Eff^{max} = 1/\theta_1 = 0.103$ the coupling efficiency at 220 kHz, for a LC circuit exactly tuned to this frequency.

For each of the n_1 LC circuits, $n_2 = 100$ forces are randomly generated with *Matlab*. The histogram is given on Figure 36.

Histogram of force 20%
Normal

Mean	6.529
StDev	1.091
N	10000
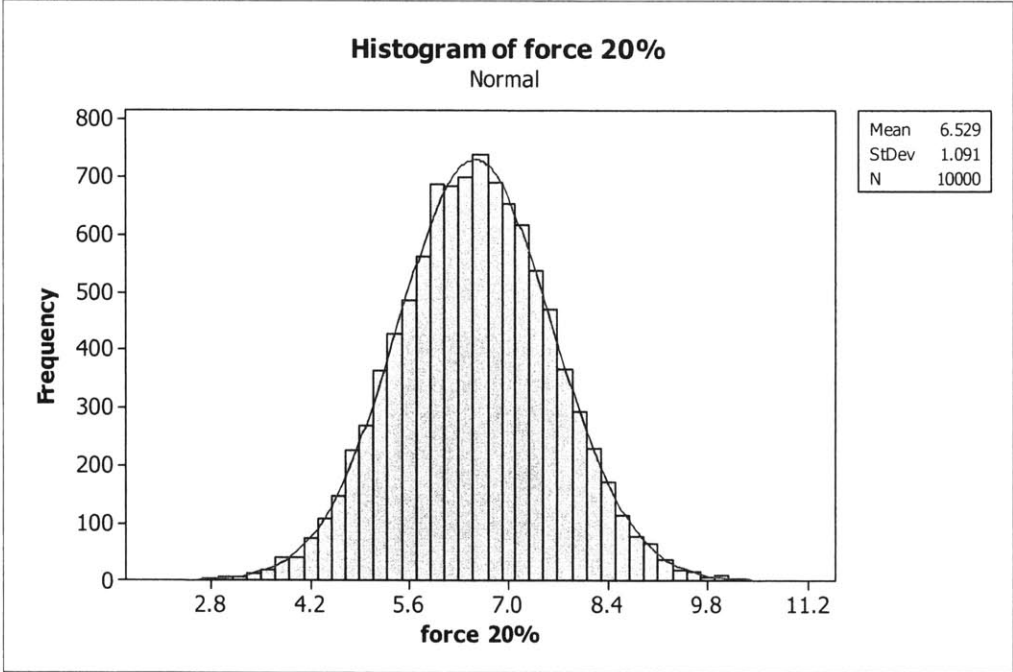
Figure 36: Histogram of the force generated by the half sized enabler

Because the force generated by the enabler at a given coupling efficiency is assumed to be normal, the final force distribution is also closed to normal. The characteristics of the distribution are summarized in Table 13.

Table 13: Force histogram summary

Mean	6.5295 N	Skewness	-0.0157
Standard Deviation	1.0909 N	Kurtosis	0.0101

95% C.I. for mean	[6.5081 ; 6.5509]
95% C.I. for standard deviation	[1.0760 ; 1.1062]

7.6. Discussion on the Component Quality

This entire simulation was run 3 times, with three different levels of capacitance quality: 5%, 10% and 20%.

Table 14: Resonant frequency distributions

Cap. Quality	5%	10%	20%
Mean	219,469 Hz	219,585 Hz	219,242 Hz
Standard Deviation	1,018 Hz	2,095 Hz	3,544 Hz
95% CI for mean	[219,266 ; 219,271]	[219,169 ; 220,000]	[218,782 ; 221,069]
95% CI for std. dev.	[894 ; 1,183]	[1,840 ; 2,434]	[3,112 ; 4,117]

Table 15: Force distributions

Cap. Quality	5%	10%	20%
Mean	6.5527 N	6.5497 N	6.5295 N
Standard Deviation	1.1005 N	1.1015 N	1.0909 N
95% CI for mean	[6.5311 ; 6.5743]	[6.5281 ; 6.5713]	[6.5081 ; 6.5509]
95% CI for std. dev.	[1.0854 ; 1.1159]	[1.0864 ; 1.1170]	[1.0760 ; 1.1062]

As expected, the standard deviation of the frequency distribution increases as the capacitor quality decreases. However, under our assumptions, it does not affect the standard deviation of the enabler force distribution. Indeed, the 95% confidence intervals for the standard deviations overlap. In the particular case of this realization, the estimate of the standard deviation for 20%-capacitor is even smaller than the 5% and 10%-capacitors. This phenomenon is attributed to the rather large manufacturing variability of the enablers. Thus, the force distribution that can be generated has a significantly higher variance than the electronic components. From this simulation, it comes that the use of 20%-capacitor would not damage the performance of the lock. However, the manufacturing variability of the enabler should be kept under control. At the time of this thesis, the enabler was indeed made by hand, in small quantities (several thousands). Manufacturing control of this part was not a priority for ProTeqt yet.

Chapter 8

Conclusions and Future Work

Our project at ProTeqt addressed various problems in the design and the manufacturing of its Micro-USB lock. They can be divided into three categories:

1. The design of the LC circuit that optimizes coupling efficiency with the primary coil,
2. The probability that the enabler fails to open the lock, and
3. The effect of LC circuit variability on the lock reliability.

Even though these three points were addressed, this thesis principally focused on the first one. For full details about the lock mechanism and the manufacturing issues, the reader can refer respectively to [19] and [20].

At the end of this project, it appears that ProTeqt is now able to reliably open a lock at a distance of one inch. Using an LC circuit resonator to repeat the magnetic field of the tablet opens a new range of application to the company. However, some research has to be pursued to make this solution fully applicable to the retail industry. The following paragraphs propose some immediate teachings from our work at ProTeqt. Then future work is detailed, both for the short and long terms.

8.1.   Recommendations

8.1.1. LC circuit design

Given the existing design of the lock, the most efficient wound coil is a 9-turn coil with a wire gage of 0.5mm. Moreover, in order to decrease the loss of coupling efficiency due to the enabler, it is recommended to decrease its current size (9mm by 12mm). As far as the tests went, using a rectangular piece of 9mm by 6mm provides much better results.

For more general considerations,

- The loss of coupling efficiency is mostly determined by the ratio of the enabler size over the coil size. It is recommended to keep the enabler smaller than the coil.

- Up to a certain point that is not studied in this thesis, an efficient coil has a large gage size and a high number of turns.

- In order to optimize the design of the circuit, one must primarily maximize the induced current through it.

If other manufacturing techniques are considered, a design change may be necessary for the coil, especially if the thickness of the conductive material is small (printing, etching ...). In this case, we would advise to consider the design proposed on section 5.7.2. In this design, the coil consists of several parallel lines. This design decreases the resistance of the coil without any over cost. However, the exact design has not been optimized yet (number of parallel lines, number of turns, thickness ...). It certainly depends on the manufacturing method.

8.1.2. Lock Mechanism

When the lock is directly on the tablet, the probability of failure of the locking mechanism is extremely low. It can be neglected with respects to the failure rate of the tablet.

At one inch above, this failure rate increases but was proven to remain sufficiently low. At this height, half-sized enabler (9mm x 6mm) is more reliable than the full-sized enabler (12mm x 9mm). Thus, the smaller enabler should be preferred for this application.

While the failure rate of the locking mechanism is extremely low, it is now crucial that the tablet is more reliable, in order to guarantee ProTeqt's success.

8.1.3. Effect of LC Circuit Variability on Lock Reliability

The quantitative analysis about the variability of the electronic components is not directly applicable. Because of tablet availability issues, the appropriate tests could not be done on time. Thus, a numerical simulation was implemented with strong assumptions. However, as far as these assumptions are reasonable, it appears that the quality of the capacitance does not significantly affect the performance of the lock. Thus, the use of 20%-capacitance should be sufficient for this application.

Then, this simulation also exhibited the predominance of the enabler manufacturing variability. Indeed, enablers are currently made by hand, in small batches. If this method is pursued for full scale production, one must be extremely careful to the manufacturing variability and verify that it cannot compromise the reliability of the lock. Similarly, this significant variability may be problematic for other applications that ProTeqt would want to develop in the near future.

In order to improve the model, we recommend ProTeqt to do a series of tests on the tablet, in order to refine the relationship between coupling efficiency and force generated by the enabler. For that, LC circuits with different natural frequencies should be used to expand enablers at one inch above the tablet.

8.2. Future Work

Drawing from the conclusions of this thesis, ProTeqt's future work can be divided into two parts: (a) the work specifically related to the micro-USB lock for 1in.-thick packages, and (b) the work for ProTeqt general business.

8.2.1. Micro-USB Lock

Concerning the coil design, other manufacturing methods could be considered, such as etching or inkjet printing. In this case, this thesis proposes an alternative design. However, it is not totally defined and substantial research still needs to be done, according to the chosen manufacturing method.

Then, more data are required to accurately evaluate the probability of failure of the lock, especially at one inch above the tablet.

Finally, we showed that the thermal mass of the enabler is extremely important in terms of lock reliability and should be minimized, as long as the enabler can provide enough force to open the lock. However, another approach may be considered to improve the heating of the enabler. Some preliminary experiments conducted at ProTeqt show that the corner of the rectangular shaped enabler might be useless thermal mass. Thus, further investigation should be done on other shapes, especially the circular shape one.

8.2.2. ProTeqt Business

More generally, two areas of development have been discovered during the time of this project. Firstly, the tablet is not reliable enough. Thus, lots of effort should be put into it to significantly decrease its failure rate.

The second area of development concerns the distance of unlocking. For this thesis, the objective was one inch. However, it must be seen as a short-term objective. Besides larger packaging, the retail industry also goes to a completely new experience at the point-of-sale. Thanks to the progress of non-contact technology, it would be possible to check-out the products without physical manipulation from

the clerk or the customer. For example, all the products a customer buys could be recognized and charged by passing his cart through an RFID reading zone. In this case, all the anti-theft lock must be opened during the check-out. Thus, the next distance objective of ProTeqt might be several feet instead of one inch only.

References

[1]   Finklea K., 2011, Organized Retail Crime, Congressional Research Service.

[2]   Centre for Retail Research, 2011, "Centre for Retail Research, Nottingham UK," The First Worldwide Shrinkage Survey.

[3]   Zahn M., 1987, RES.6-002 Electromagnetic Field Theory: A Problem Solving Approach, Spring 2008. (Massachusetts Institute of Technology: MIT OpenCourseWare), License: Creative Commons BY-NC-SA.

[4]   Sutton R. M., 1938, Demonstration experiments in physics, McGraw-Hill company inc.

[5]   Lee Y. L., and Sorrells P., 2004, MicroID 125 kHz RFID System Design Guide.

[6]   Finkenzeller K., 2003, RFID Handbook: Fundamentals and Applications in Contactless Smart Cards and Identification, John Wiley & Sons, Inc.

[7]   Schauber M. J., Newman S. A., Goodman L. R., Suzuki I. S., and Suzuki M., 2007, "Measurement of mutual inductance from frequency dependence of impedance of AC coupled circuits using a digital dual-phase lock-in amplifier E ~ Lock-in ampliier," American Journal of Physics, **76**(2).

[8]   Tesla N., 1900, "Apparatus for transmission of electrical energy."

[9]   Kurs A., Karalis A., Moffatt R., Joannopoulos J. D., Fisher P., and Soljacic M., 2007, "Wireless power transfer via strongly coupled magnetic resonances.," Science (New York, N.Y.), **317**(5834), pp. 83–6.

[10]   Karalis A., Kurs A. B., Moffatt R., Joannopoulos J. D., Fisher P. H., and Soljacic M., 2009, "Wireless energy transfer," US Patent 8097983, **2009**, pp. 1045–8.

[11]   Georgakopoulos S. V., and Jonah O., 2011, "Optimized wireless power transfer to RFID sensors via magnetic resonance," 2011 IEEE International Symposium on Antennas and Propagation (APSURSI), pp. 1421–1424.

[12]   Cannon B., and Hoburg J., 2009, "Magnetic resonant coupling as a potential means for wireless power transfer to multiple small receivers," IEEE Transactions on Power Electronics, **24**(7), pp. 1819–1825.

[13]   Beckwith L., 2013, "Inductor Theory," General Linear Systems.

[14]   Lee Y., 1998, RFID Coil Design.

[15]   Universe P., 2013, "Printed circuit boards," PCB Universe [Online]. Available:
         http://www.google.com/patents?hl=en&lr=&vid=USPAT4751146&id=9IIyAAAAEBAJ&oi=fnd&dq=
         Printed+Circuit+Boards&printsec=abstract. [Accessed: 27-Jul-2013].

[16]   SAWYER A., 2010, "Fabrication of nanofluidic devices using electrochemical etching of sacrificial
         copper."

[17]   Numakura D., 2008, "Advanced Screen Printing 'Practical Approaches for Printable and Flexible
         Electronics'," 2008 3rd International Microsystems Packaging Assembly Circuits Technology
         Conference, pp. 205–208.

[18]   Hoban M., and Lunt B., 1997, "Soldering," The Technology Interface, **26**(5) [Online]. Available:
         http://www.ncbi.nlm.nih.gov/pubmed/23822908.

[19]   Zhu T., 2013, "Design and Manufacturing Analysis of Resonantly Coupled Circuits and Other
         Components used for Wireless Benefit-Denial System," Massachusetts Institute of Technology.

[20]   Krogman M., 2013, "Design and Manufacturing Analysis of Resonantly Coupled Circuits and Other
         Components used for Applied Wireless Power Transmission: Application Analysis."

[21]   Lee Y. L., and Sorrells P., 2004, MicroID 125 kHz RFID System Design Guide.

[22]   Mur-Miranda J. O., Fanti G., Feng Y. F. Y., Omanakuttan K., Ongie R., Setjoadi A., and Sharpe N.,
         2010, Wireless power transfer using weakly coupled magnetostatic resonators.

Appendix

A. Theoretical Calculation of Resistance and Geometric Factor

In this section, the diameter of a wire is called d_w and the number of turns of the coil is N. d_{in} is the inner diameter of the coil. The coil is seen as N concentric circles, as shown on Figure 37.
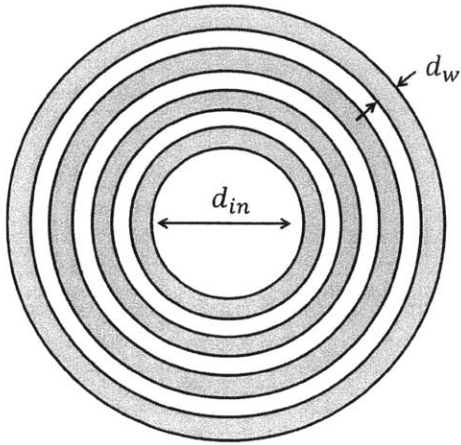

Figure 37: Equivalent Coil Model

In this case, space between turns is neglected.

A.1.   Resistance

The DC resistance R of a conductive wire is defined by the following relationship:

$$R = \frac{\rho L}{A} \tag{A.1}$$

where ρ is the resistivity of the material (for copper, $\rho = 1.72 \times 10^{-8} \Omega.m$), L is the length of the wire and A is the cross section area of the wire.

Considering the assumption about the coil geometry, the length of the wire is the sum of the length of each turn (sum of the terms of an arithmetic sequence).

$$L = \pi N(d_{in} + N d_w) \tag{A.2}$$

The cross section area comes directly from the gage size:

$$A = \pi \frac{d_w^2}{4} \tag{A.3}$$

As we deal with AC current, the resistance can be refined, by taking into account the skin effect in the wire [21]. If the frequency is high enough so that the skin depth δ is small compared to the wire diameter, the effective resistance is given by:

$$R_{eff} = \rho \frac{L}{\pi d_w \delta} \qquad (A.4)$$

Otherwise, the resistance is

$$R_{eff} = R_{DC} \left(1 + \frac{1}{48} \left(\frac{d_w}{2\delta} \right)^2 \right) \qquad (A.5)$$

A.2. Geometric Factor

The geometric factor A is numerically calculated from the formula below:

$$A = \sum_{i=1}^{N} \pi \frac{d_i^2}{4} = \sum_{i=1}^{N} \pi \frac{\left(d_{in} + d_w (2i - 1) \right)^2}{4} \qquad (A.6)$$

A.3. Spreadsheet

Material properties			
resistivity	ρ	1.72E-08	Ohm.m
frequency	f	220	kHz
		2.20E+05	Hz
permeability	μ	1.26E-06	H/m
skin depth	δ	0.000140726	m
		0.140725569	mm

Figure 38: Material Properties (input). Here, copper.

Coil characteritics			
number of turns	N	9	turns
inner diameter	din	4	mm
		4.00E-03	m
outer diameter	dout	1.22E-02	m
		12.176	mm
total length	L	2.43E-01	m
Gage	AWG	24	
wire dimaeter	d_w	0.511	mm
		5.11E-04	m

Figure 39: Coil Characteristics (input)

Resistance		
DC resistance	2.04E-02	Ω
	20.39	mΩ
Eff. Resistance	2.18E-02	Ω
low freq	2.18E-02	Ω
high freq	1.85E-02	Ω

Figure 40: Resistance of the wire

Geometric Factor		
A	0.00117125	m^2

Figure 41: Geometric Factor of the Coil
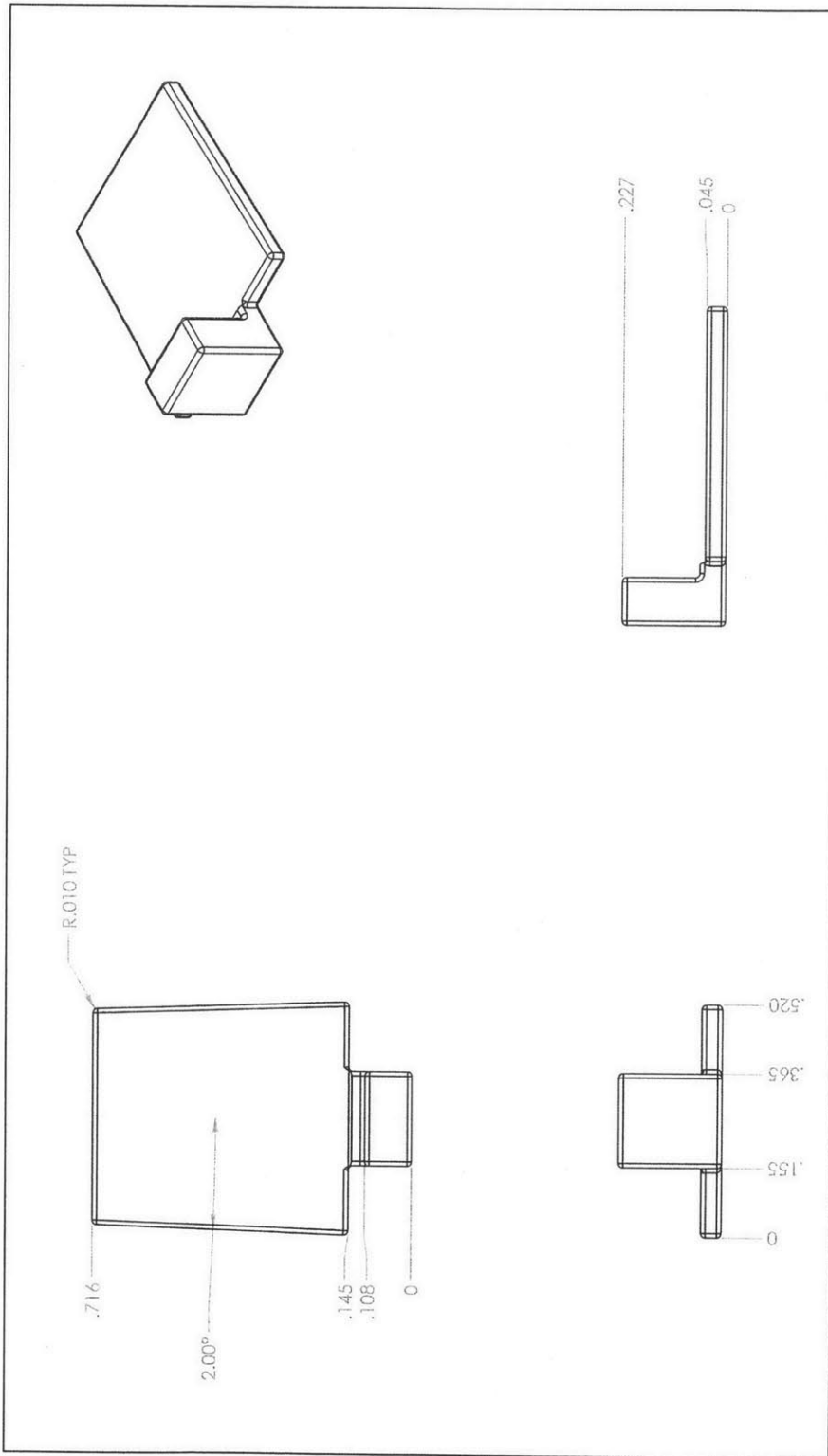
B. Drawing of LC Circuit Site inside the Lock.

Figure 42: Drawing of LC circuit location inside the lock. Unit is inch.

C. Current Estimation in the Secondary Circuit

For the purpose of experiments, we will need to have an idea of the induced current passing through the secondary circuit. The most direct way to measure current is to know the voltage in a resistor. The current passing through a resistor is proportional to its voltage. However, it is impossible to introduce a serial resistor in the secondary circuit since it would strongly decrease the efficiency of the coupling [22]. Finally, the following method was proposed to estimate current passing through the secondary circuit. The magnetic field from the primary coil induced eddy current $\underline{I}$ in the LC circuit:

$$\underline{I} = I_{RMS}e^{j\omega t} \tag{C.1}$$

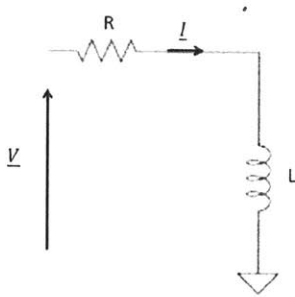We represent the actual coil by an ideal inductance L in series with a small resistance R (see Figure 43).

Figure 43: Electric Model of the Coil

Using complex notation:

$$\underline{V} = R\,\underline{I} + j\omega\,L\underline{I} = I_{RMS}(R + j\omega L)e^{j\omega t} \tag{C.2}$$

So finally,

$$V_{RMS} = |\underline{V}| = I_{RMS}\sqrt{R^2 + (\omega L)^2} \tag{C.3}$$

We measure the voltage peak-to-peak V_{pp}. Thus,

$$V_{RMS} = \frac{V_{pp}}{2\sqrt{2}} \tag{C.4}$$

As $\omega = 2\pi f$, we can get the RMS value of the current:

$$I_{RMS} = \frac{V_{pp}/2\sqrt{2}}{\sqrt{R^2 + (2\pi f L)^2}}$$

(C.5)

The value of the current should not be considered as exact. This is only an estimate. First, the resistance is the DC resistance of the coil and does not take into account the increase of the resistance with frequency. Then, inductance is measured at 1 kHz and 0.25 V, which is not the condition of the test. Finally, this simple model does not take into account the voltage induced by electromagnetic coupling (see section 4.1 and 4.2). This voltage is however assumed to be small when the two antennas are 1 inch apart, because coupling is weak.[22]

D. Frequency Shift due to Distance

Each circuit is tuned to a specific frequency, called natural frequency, and determined by the values of the inductance and the capacitance. However, preliminary experiments of coil coupling consistently exhibited a downward shift of the natural frequency. To understand the cause of this frequency shift, we go back to the theoretical analysis of resonant inductive coupling (see section 4.1). Let be V_{C_2} the voltage in the capacitor of the secondary circuit. Thus,

$$V_{C_2} = \frac{i_2}{j\omega C_2} \tag{D.1}$$

Then, combining equation (D.1) with equations (4.5) and (4.6) (see page 38), the ratio of the output voltage over the input voltage is

$$\frac{V_2}{E} = \frac{M}{C_2 \left(Z_1 \cdot Z_2 - \omega^2 M^2 \right)} \tag{D.2}$$

with $\omega = 2\pi f$, $Z_1 = R_1 + j\omega L_1$, $Z_2 = R_2 + j\left(\omega L_1 - \frac{1}{\omega C_2} \right)$ and $M = k\sqrt{L_1 L_2}$, $0 \le k \le 1$.

This voltage ratio is plot for various values of k, on Figure 44. The values of the electrical components are $R_1 = 7\ m\Omega$, $L_1 = 1.19\ \mu H$, $R_2 = 23.7\ m\Omega$, $L_2 = 0.63\ \mu H$ and $C_2 = 1\ \mu F$. For these set of numerical values, the natural frequency of the secondary LC circuit is

$$f_0 = \frac{1}{2\pi\sqrt{L_2 C_2}} = 200\ kHz \quad or \quad \omega_0 = \frac{1}{\sqrt{L_2 C_2}} = 1.26 \times 10^6\ rad.s^{-1}$$
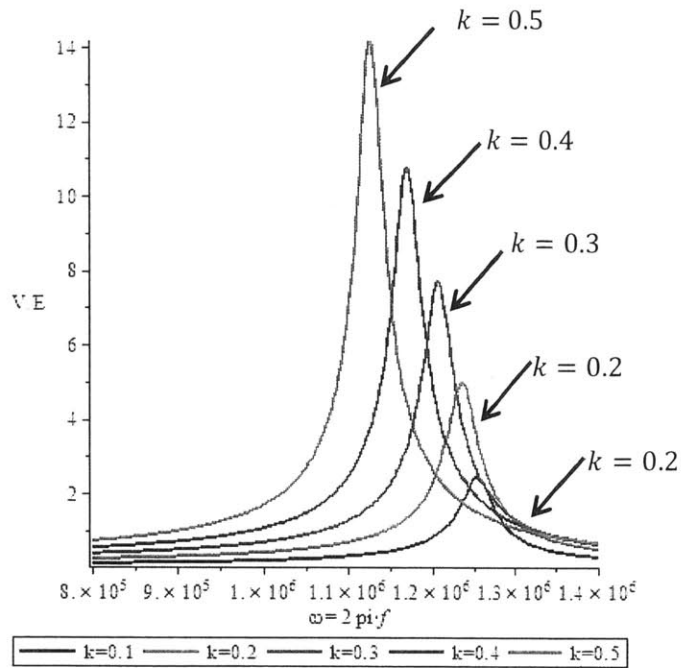
Figure 44: Voltage ratio of inductive coupling, for several values of the coupling coefficient

Figure 44 confirms the preliminary observation. The resonance peak shifts downward when the quality of coupling increase (typically when the two coils get closer). To illustrate the relationship between the resonant frequency and the coupling coefficient, we can refer to Figure 45.
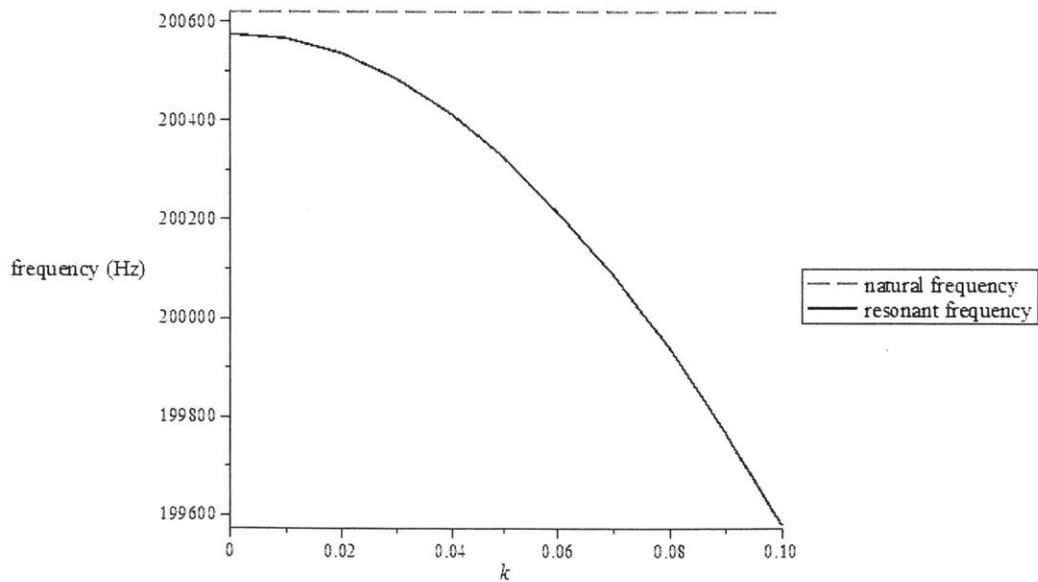

Figure 45: Resonant frequency of the coupling versus the coupling coefficient. Dash line is the natural frequency of the secondary LC circuit.

91

In case of inductive coupling (i.e. $M \neq 0$), the resonant frequency is smaller than the natural frequency of the secondary circuit. Moreover, the resonant frequency increases as the coupling quality decreases. Thus, the difference between natural and resonant frequencies is expected to decrease as the distance between the two coils increases. However, the calculation predicts a residual gap between both frequencies, as soon as the slightest inductive coupling occurs. For the graph on Figure 45, the smallest coupling coefficient was $k = 10^{-24}$.

Figure 46: List of Manufactured Coils

	1	2	3	4	5			6
Layer	one	two	one	three	one	one	one	一层
OD (in) (mm)	0.35*0.47 (8.9*12)	0.35*0.47 (8.9*12)	0.35*0.47 (8.9*12)	0.35*0.47 (8.9*12)				0.493*0.541 (12.5*13.7)
Wire Gauge	φ0.32mm	φ0.32mm	φ0.5mm	φ0.2mm	φ0.5mm	φ0.32mm	φ0.2mm	φ0.5mm
Number of turns (TS)	9	16	6	47	9	9	9	9(内孔稍大点)
Picture								
Inductance (uH) 1KHZ 0.25V	0.61	1.7	0.25	14.25	0.63	0.616	0.61	0.72
Resistance (mΩ)	46.1	79.1	13.4	586	23.7	47	96	24.9

F. Analytical Force Calculation

This analysis used a typical beam-bending model to simulate the forces required by the lock. Overall, the analytical calculations also took frictional forces, as applied by the spring, into account, making it a more robust analysis of the lock. That is:

$$F_{Total} = F_{Friction} + F_{Bending} \tag{F.1}$$

$F_{Friction}$ can be defined as:

$$F_{Friction} = \mu F_{Spring} \tag{F.2}$$

$$F_{Spring} = k(x_0 - x) \tag{F.3}$$

$$k = \frac{Gd^4}{8D^3 n_a} \tag{F.4}$$

$$G = \frac{E}{2(1 + v)} \tag{F.5}$$

Where μ is the coefficient of friction between the two stainless steel components, k is the spring rate, x_0 is the free length of the spring, x is the displaced distance of the spring, G is the shear modulus of the spring, d is the diameter of the wire, D is the spring diameter, n_a is the number of turns in the spring, E is young's modulus for the spring material, and v is Poisson's ratio.

$F_{Bending}$ can be defined using the following model:
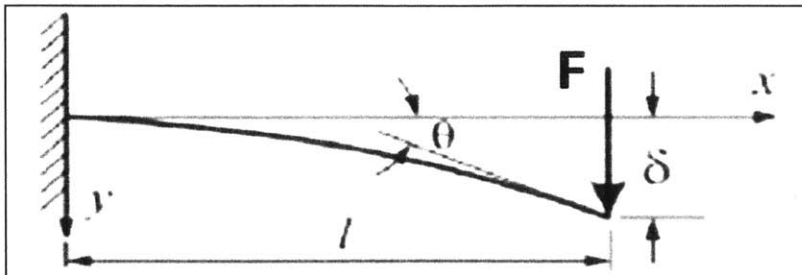

Figure 47: Beam bending model used for analytical calculations.

$$F_{Bending} = \delta(x)\frac{6EI}{x^2(3L-x)} \qquad (F.6)$$

where $\delta(x)$ is the displacement at point x, E is Young's modulus of the sheet metal, I is inertia, L is the length of the beam, and x is the position at which the force is applied.

The following tables list the values used to complete the analytical calculations.

Table 16: Spring force calculation

Spring Force						
μ	0.8			Spring properties		
k	5.25E+02	N/m		G	6.90E+10	Pa
x	0.007461	m		E	1.80E+11	Pa
x_0	2.40E-02	m		d	3.60E-04	m
x_0-x	1.65E-02	m		D	2.64E-03	m
				na	15	

Table 17: Bending force Calculation

Bending Force						
δ	4.34E-04	m		Beam Properties		
x	5.00E-03	m		E	1.80E+11	Pa
				L	5.21E-03	m
				I	1E-14	m^4

Using the values listed above for each parameter in the equation for the frictional component, we have:

$$F_{Spring} = k(x_0 - x)$$

$$F_{Spring} = 8.68N$$

$$F_{Friction} = \mu 8.68N$$

$$F_{Friction} = 6.94N$$

Also, we compute the bending component as:

$$F_{Bending} = \delta(x)\frac{6EI}{x^2(3L-x)}$$

$$F_{Bending} = .000434 \frac{6 * (1.80E + 11) * (1E - 14)}{0.005^2(3 * 0.00521 - 0.005)},$$

$$F_{Bending} = 17.7N$$

In conclusion, we sum the two force components to obtain the total force required to disengage the lock. The sum of the two forces is 24.6N.